FRONTIERS OF PHYSICS

TOPICAL REVIEW
Volume 19 / Issue 6 / 62502 / 2024

# Emerging single-photon detection technique for high-performance photodetector

Jinxiu Liu[1], Zhenghan Peng[1,2], Chao Tan[1], Lei Yang[1], Ruodan Xu[3], Zegao Wang[1,†]

1 College of Materials Science and Engineering, Sichuan University, Chengdu 610065, China
2 Department of Materials Science and Engineering, Stanford University, California 94305, USA
3 Department of Biomedical Engineering and Technology, Institute of Basic Theory for Chinese Medicine, China Academy of Chinese Medical Sciences, Beijing 100700, China
Corresponding author. E-mail: †zegao@scu.edu.cn
Received March 19, 2024; accepted May 27, 2024



## ABSTRACT

Single-photon detections (SPDs) represent a highly sensitive light detection technique capable of detecting individual photons at extremely low light intensity levels. This technology mainly relies on the mainstream SPDs, such as photomultiplier tubes (PMTs), avalanche photodiodes (SAPD), superconducting nanowire single-photon detectors (SNSPDs), superconducting transition-edge sensor (TES), and hybrid lead halide perovskite. However, the complexity and high manufacturing cost, coupled with the requirement of special conditions like a low-temperature environment, pose significant challenges to the wide adoption of SPDs. To address the challenges faced by SPDs, significant efforts have been devoted to enhancing their performance. In this review, we first summarize the principles and technical challenges of several SPDs. Conductors, superconductors, semiconductors, 3D bulk materials, 2D film materials, 1D nanowires, and 0D quantum dots have all been discussed for single-photon detectors. Methods such as special optical structure, waveguide integration, and strain engineering have been employed to elevate the performance of single-photon detectors. These techniques enhance light absorption and modulate the band structure of the material, thereby improving the single-photon sensitivity. By providing an overview of the current situation and future challenges of SPDs, this review aims to propose potential solutions for photon detection technology.

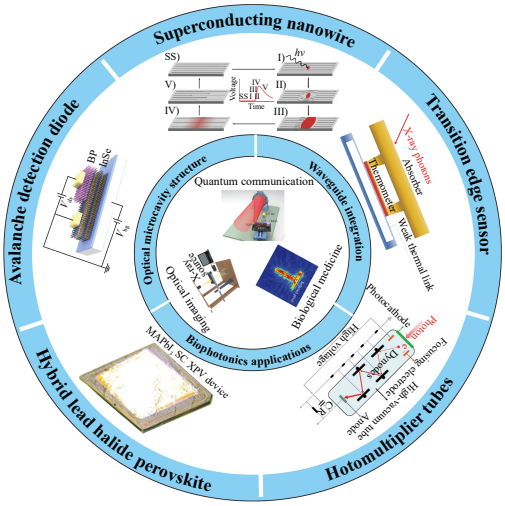


**Keywords** single-photon detection, superconductor, semiconductor, low dimensional materials, optical structure, waveguide integration, strain engineering

## Contents



Higher Education Press

https://doi.org/10.1007/s11467-024-1428-1

# 1 Introduction

Traditional photoelectric detection uses photons with energy greater than the band gap being incident on the detection area of the device, resulting in the generation of photon current. However, in single-photon detection, when the light power is relatively weak, the incident photon beam presents as discrete states, arriving at the detector in the form of particles. As a result, conventional photoelectric detection technologies exhibit reduced responsive, increased noise, and requires continuous scattering [1]. The number or intensity of incident photons in SPDs can be measured through the photoelectric detector. Photoelectric detectors converts optical signals into electrical signals to detect the intensity and frequency of radiation signals and are widely used in quantum communication [2–4], optical imaging [5–9], biomedicine [10–13], remote detection [14–16], and defense military [6, 17]. These detectors can convert the received single photon's energy into an electrical signal, enabling efficient detection of very low light intensity signals. SPDs facilitate the migration of photogenerated carriers to the detector multiplier region by electric field acceleration. Under certain conditions, the photogenerated carriers undergo collision ionization with the lattice in the multiplier region, continually produce new photogenerated carriers [18]. Compared with traditional photoelectric detection, SPDs have the following advantages: weak light detection and ultra-high time resolution, which can be far lower than the pulse width of a photomultiplier tube. Future single photon detection technology will face the following challenges: (i) Higher operating temperature of single photon detection to reduce equipment and material costs. (ii) Manufacture larger detection arrays at the centimeter level or larger scale. (iii) Wider detection wavelength (middle-far infrared band). (iv) More extreme environment detection, such as long-range detection, deep space optical communication, and underwater detection.

# 2 Working mechanisms of single photon detector

## 2.1 Single photon avalanche detection diode

### 2.1.1 Principle of single photon detection avalanche diode

Single photon avalanche diode (SPAD) is a p–n junction that operates in Geiger mode. The device operates with a bias voltage significantly higher than its reverse bias breakdown voltage, rendering it versatile for a wide range of applications due to its excellent sensitivity to both photons and charged particles. This technology is well developed and commercially available in the short infrared range. The mechanism of avalanche diode photodetection is shown in Fig. 2(a), the photon is absorbed in the P-type region, producing electron-hole pairs. Currently, avalanche diodes are advancing rapidly in two directions: one path is to continuously optimize the performance of existing InP/InGaAs-SPAD-like block avalanche towards the smaller dark count, lower after-pulse effect, higher count rate, and higher operating temperature. The other path is finding more promising new materials and mechanism devices. Therefore, novel materials and new mechanism devices capable of achieving high gain multiplication have emerged. Those include low noise materials with low $k$-factor, low dimensional materials that can extend wavelength ranges, ballistic transport of low dimensional materials, and separation multiplication engineering to reduce noise.

When the SPAD operates in Geiger mode, excessive induced current will damage the device's performance and reduce the detection efficiency for a long time. To optimize and expand the application of the avalanche diode, it must be supported by the quenching circuit

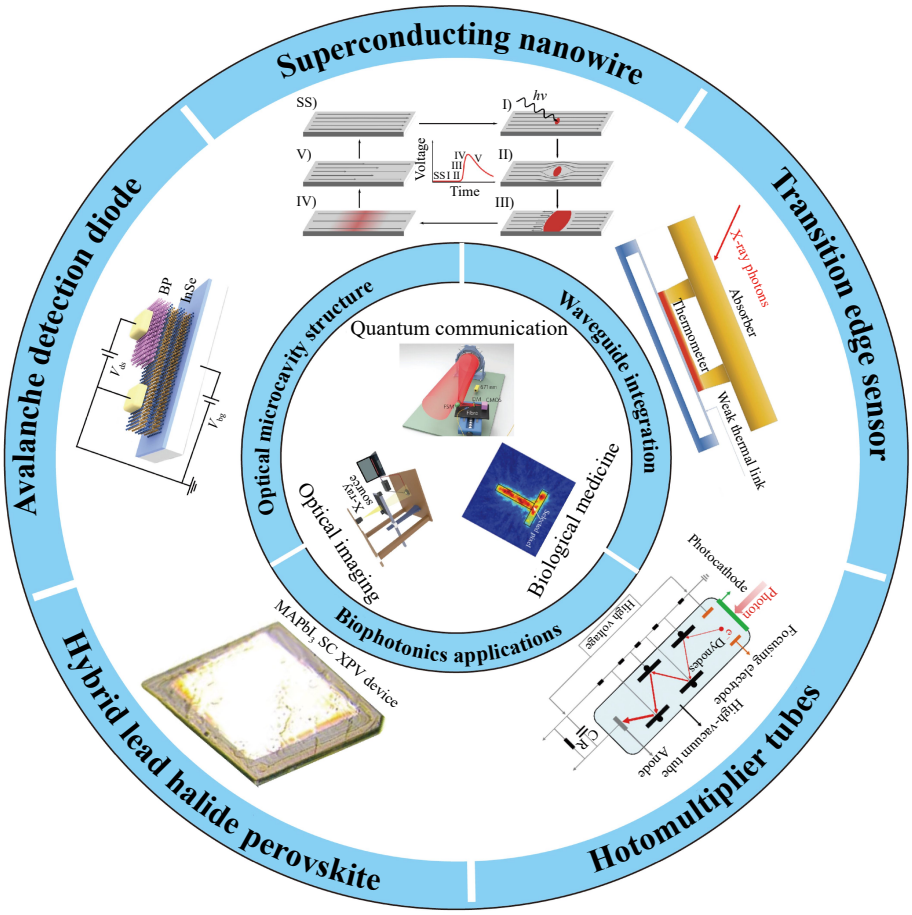


**Fig. 1** Scope of this review.

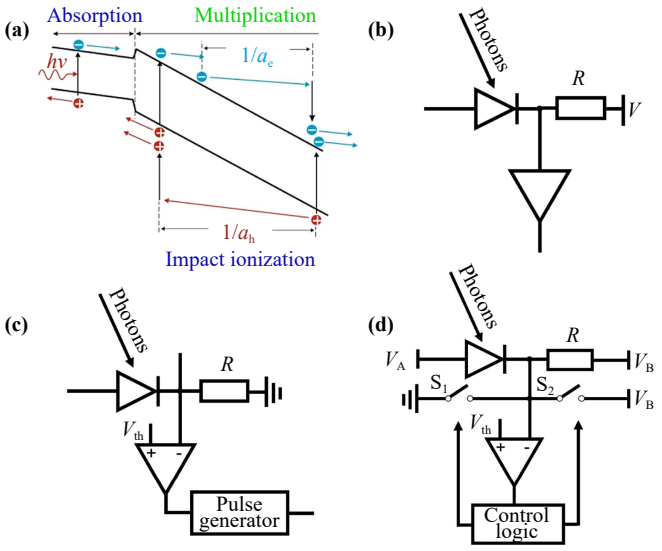


**Fig. 2** **(a)** Schematic diagram of the multiplication effect in APD. Reproduced from Ref. [19]. Avalanche diode quenching circuit: **(b)** passive quenching, **(c)** active quenching, and **(d)** mixed quenching.

[20]. On the one hand, the quenching circuit needs to stop the avalanche in time, on the other hand, it also suppresses the noise from the device and circuit to extract the avalanche signal. At present, the main idea of the quenching circuit is to extract a digital pulse signal upon detecting avalanche current and subsequently quench the current by applying an extra reverse bias. The quenching mode can be divided into "passive quenching" in Fig. 2(b), "active quenching" in Fig. 2(c), and "mixed quenching" in Fig. 2(d). As shown in Fig. 2(b), passive quenching is realized automatically by current limiting and voltage division of resistance above 100 kΩ, which is faster and more convenient. The disadvantage is that the added "large resistance" makes the device unsuitable for array line SPAD. Active quenching in Fig. 2(c) is to forcibly reduce the avalanche effect of SPAD's reverse bias voltage by additional control structure after the avalanche current is detected, and the reaction time is fast. However, due to the large capacitance constant in the circuit, the photon count of SPAD is lower than 100 kHz. The mixed quenching mode is more complex and is not often used as shown in Fig. 2(d). Through the above three quenching modes, the dark count and after-pulse of the device are significantly reduced, and the counting rate of the device is improved.

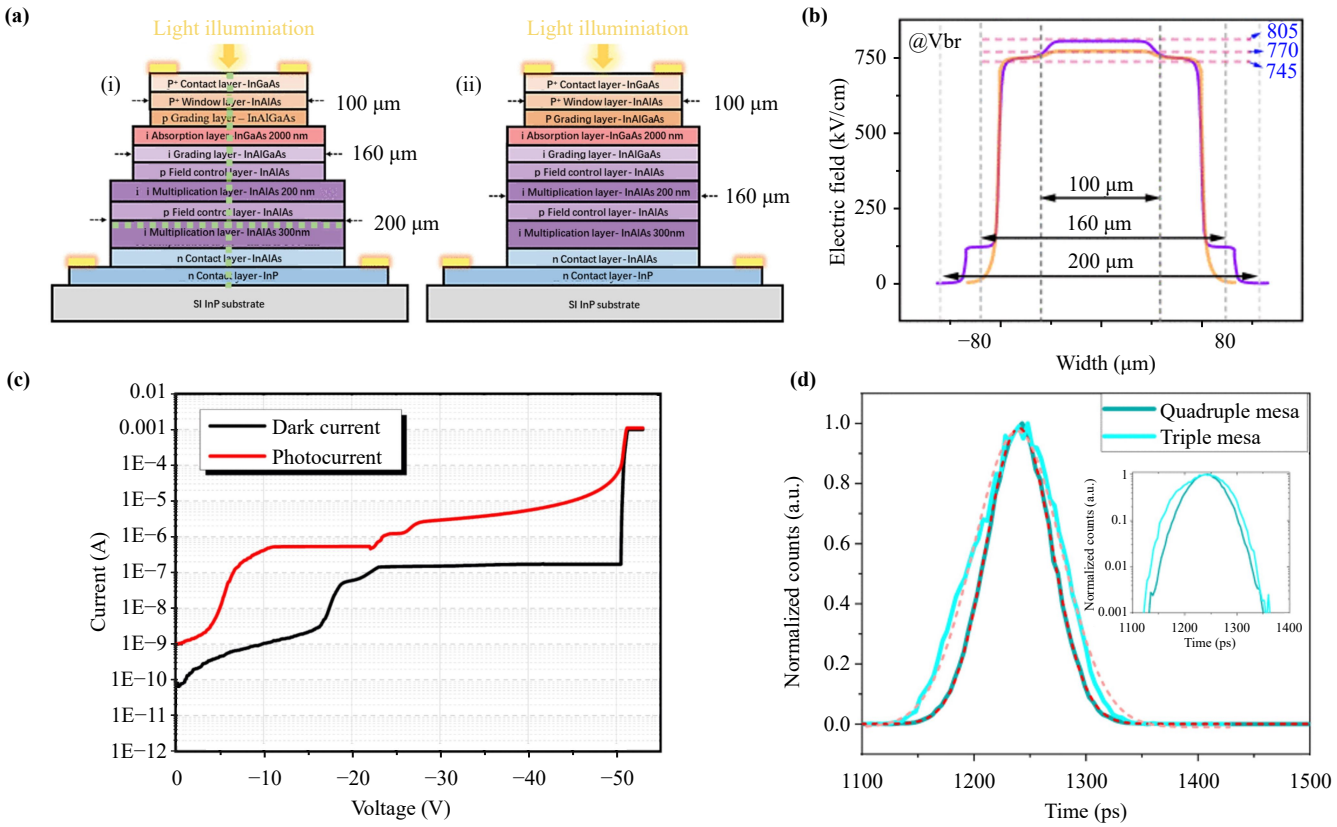


**Fig. 3** Multiple multiplication layer avalanche diode. **(a)** Illustration of InGaAs/InAlAs-SPAD with quadruple mesa structure (i) and triple mesa structure (ii). **(b)** Transverse electric field profile of the lower side of the second multiplication layer. **(c)** Dark current and photocurrent of mesa-type InGaAs/InAlAs SPAD illuminated with an optical power of 1 μW. **(d)** Gaussian-like temporal responses were measured at $T = 200$ K for quadruple and triple mesa devices. Reproduced from Ref. [31].

### 2.1.2 SPAD based on conventional bulk semiconductors

The most common bulk materials in the practical application of SPAD are Si-SPAD [21, 22], InGaAs-SPAD, InGaAs/InP-SPAD [23, 24], InAlAs-SPAD [25, 26], HgCdTe-SPAD [27], etc. The earliest and most widely used materials for short infrared and visible light are Si-SPAD and InGaAs-SPAD. Haitz *et al.* [28] developed the first batch of Si-SPAD operating in Geiger mode in 1963. Si-SPAD is favored by all parties because of its high detection efficiency, small size, and strong stability. However, due to a large electronic band-gap, it cannot be exploited for single-photon detection at a wavelength over 1000 nm. To overcome this limitation, one strategy is to convert infrared photons to higher energy photons within visible range, thereby enabling the utilization of silicon SPADs in such applications [29]. A fiber pigtail periodically polarized lithium niobate (PPLN) waveguide absorbs photons mixed with a strong pump signal of 1950 nm in the telecommunication band, which are then collected and detected by a silicon avalanche photodiode (SPAD) and frequency-generated (SFG) photons [29, 30]. Si-SPAD thick junction SPAD has high detection efficiency, but poor timing jitter. The timing jitter of shallow SPAD is good, but their detection efficiency is relatively low. To reduce the operating voltage, a smaller time jitter must be achieved at the expense of detection efficiency. All commercially available avalanche diodes use a mesa structure. For example, in Fig. 3(a), Lee *et al.* [31] adopted the concept of dual multiplication layer to construct three-layer and four-layer InGaAs/InAlAs-SPAD single-photon avalanche diodes, and the InGaAs/InAlAs-SPAD mesa devices show obvious avalanche effect as seen in Fig. 3(b), effectively reducing the dark count rate and after-pulse effect. Since avalanche triggering depends on the electric field distribution in the multiplication layer, the multi-stage table structure can effectively limit the high electric field in the central active multiplication region. Through the comparison of Fig. 3(b), it is found that the electric field in the central multiplication area of the quadruple mesa structure is higher, which can realize the effective control of the electric field. As illustrated in Fig. 3(c), compared with the triple mesa structure, the time jitter of the quadruple mesa structure is significantly reduced. Therefore, the mesa structure is widely used to better confine the distribution of electric field in the central

doubling region and further optimize the detection efficiency and timing jitter.

### 2.1.3 SPAD based on low-dimensional materials

Currently, the majority of avalanche diodes are made from bulk materials, with limited research conducted on thin film materials, which also limits the shift of the detection wavelength of avalanche diodes to the mid-far infrared. Low dimensional materials meet the growing need focus on longer wavelengths due its narrow bandgap materials such as Graphene, $WS_2$ [32], $MoTe_2$ [33], $PdSe_2$ [34], $PtTe_2$ [35], $PtSe_2$ [36, 37], and $PdTe_2$ [38]. However, as the band gap decreases, large background noise and dark count rate also occur. Dark counting is caused by factors such as low energy band gap, lattice mismatch and dislocation of materials, resulting in false photon counts generated in the absence of photon irradiation. Currently, the most effective method for reducing dark counting is to significantly reduce the operating temperature, but this also leads to increased costs. The occurrence of avalanche diodes relies on the distance over which electrons in the material accelerate, making low-dimensional materials relatively less explored in this field. Due to the atomic thickness, the inherent detection capability of low-dimensional materials photodetectors is low, and will also produces a large noise current, which further limits the detection capability. To further improve performance, it has been documented that single photon detection performance can be achieved in low-dimensional materials by introducing photogating effect, double gate modulation, ballistic avalanche, etc.

**Zero-dimensional materials (0D materials)**. Quantum dot (QD) based devices are an emerging class of promising single-photon detectors (SPDs). This kind of detector operates at a relatively low voltage bias with very low dark count rates, and has reduced noises due to the avoidance of involving the avalanche multiplication process. By adjusting the composition and size of quantum dots, the detection band can be adjusted from infrared to UV-visible. Mahdi *et al.* [39] proposed an avalanche quantum dot infrared photodetector (AQDIP) that could be a perfect candidate for detecting mid-far infrared wavelengths as shown in Fig. 4(a). The QDs layer will absorb a single photon, resulting in the generation of photogenerated electrons, which are injected and multiplied, resulting in a large output pulse signal. Figure 4(b) shows the relationship between the calculated detection efficiency and the normalized bias voltage. As demonstrated, the detection efficiency (DE) increases with the increase of bias voltage, but it is low compared to the conventional NIR SPDs. This can be explained since the effective absorption length of the QDs absorption layer is much lower than that of the bulk material. The overall optical properties of QDs-SPD exhibit improvement with decreasing temperature, as depicted in Fig. 4(c). However, excessively high bias and temperature will increase the detection efficiency while simultaneously increase the dark count rate (DCR). At higher temperatures, the quantum dot layer will experience an increment in thermally excited electrons, leading to an increase in the dark count rate. Therefore, the working temperature of the detector is limited to less than 150 K.

**One-dimensional materials (1D materials).** Positive or negative light responses can be caused by the surface states of nanowires through the photo-gating effect. Those surface states can also act as optically addressable floating gates similar to quantum dots [40]. In Fig. 4(d), Luo *et al.* [41] constructed a core-shell structure room temperature field effect transistor using cadmium sulfide single crystal nanowires. By using the photo-gating effect shown in Figs. 4(e, f), the scattering effect from the negative reverse gating voltage to the core was alleviated, and the single-photon detection efficiency of 23% was achieved in Fig. 4(g).

**Two-dimensional materials (2D materials).** 2D materials have a fascinating development potential in the field of single photon detection due to the unfavorable integration of bulk materials and the high avalanche breakdown voltage. 2D materials such as graphene, transition metal dihalides (TMDs), black phosphorus (BP), and hexagonal boron nitride (h-BN) play important roles in the field of optoelectronic detection because of their special properties, such as strong light-matter interactions, thickness-dependent electronic and optical properties, and the ability to form mixed structures [42, 43]. Single-layer graphene can produce a good light response to the ultra-wide spectral range of 300–2500 nm, with ultra-high room temperature mobility up to 1500 $cm^2 \cdot V^{-1} \cdot s^{-1}$, ultra-wide spectral detection capability, and fast response speed, but with ps level carrier lifetime and poor light absorption capacity (~2%). The band structure of graphene poses a challenge of the realization of photodetectors with a high signal-to-noise ratio [44]. The experimental challenge in building high-resolution photonics counting devices with graphene arises from the generation of substantial flicker noise in the detection (or receiver) electronics due to large bias current. In 2013, the single-layer $MoS_2$ photodetector prepared by Lopez-Sanchez *et al.* [45] demonstrated not only a very high photoresponsivity (880 A/W) but also a wide spectral range (400–680 nm). In the same year, Zhang *et al.* [46] explored the Coulomb potential of charged impurities in air on single-layer $MoS_2$ surfaces or $MoS_2/SiO_2$ interfaces, resulting in enhanced carrier scattering and reduced mobility. In 2018, Roy *et al.* [47] constructed a double-gated detector with single-photon counting ability by using double-layer graphene and $MoS_2$. By opening the band gap in the double-layer graphene, it can achieve extremely low noise (0.07 Hz) and large optical gain ($10^{10}$) at 80 K. In 2018, Liu *et al.* [48] utilized $MoS_2$ and periodically aligned graphene to

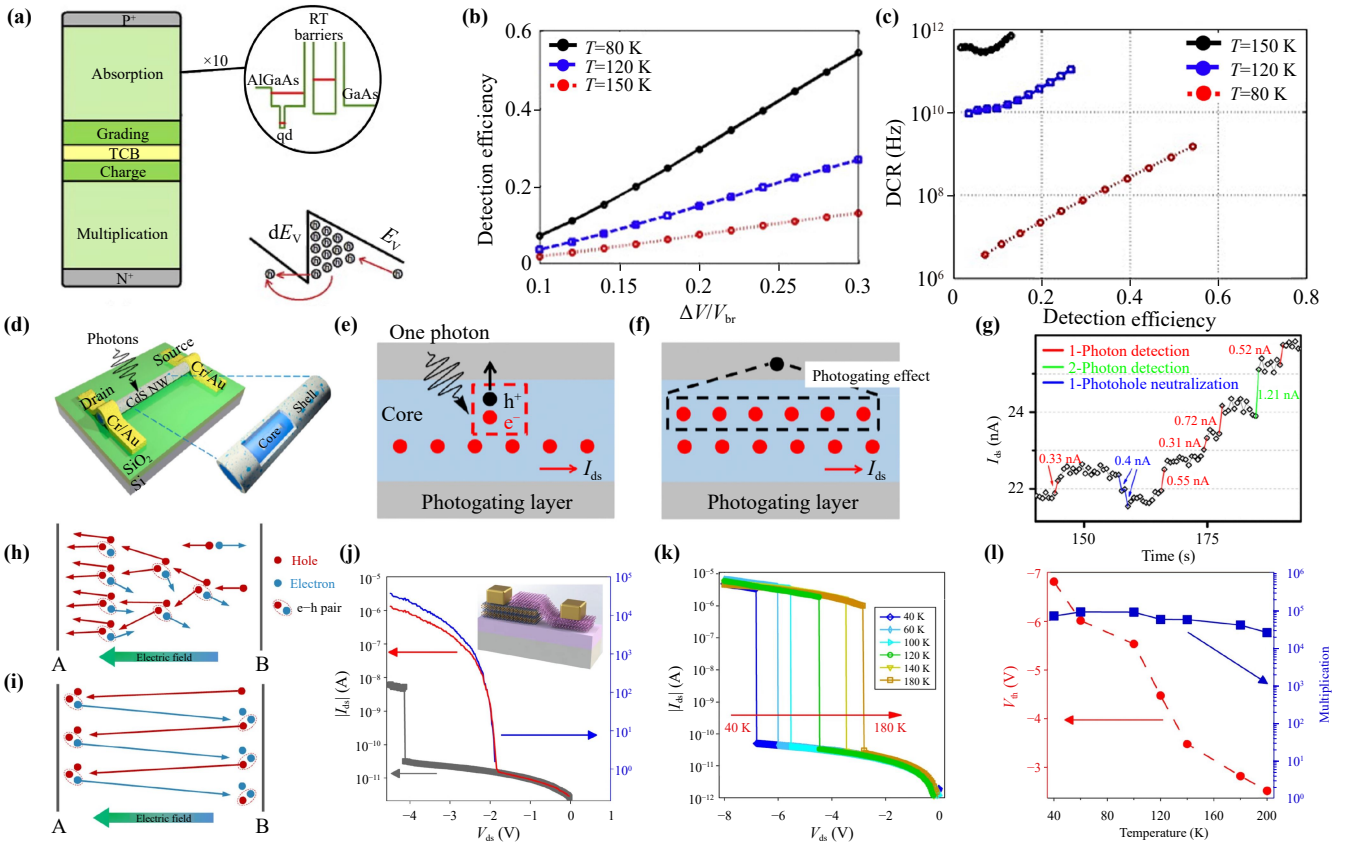


**Fig. 4** 0D quantum dot based avalanche diode. **(a)** Schematic diagram of AlGaAs/GaAs quantum dot avalanche diode single-photon detector. **(b)** Detection efficiency of AQDIP-SPD at different temperatures. **(c)** DCR of the detector as a function of its detection efficiency for different temperatures. 1D nanowires based detector. **(d)** Schematic diagram of single photon detection of CdS nanowires deposited on $Si/SiO_2$ structures. **(e)** The process of electron–hole pair induction by a single photon. **(f)** The photogating effect was induced by the trapped hole in the photogating layer. **(g)** Time-resolved of current measurements at room temperature. 2D ballistic avalanche diode. **(h)** Illustration of the conventional avalanche diode and **(i)** ballistic avalanche diode in the vertical InSe/BP heterostructure devices. **(j)** Low temperature (10 K) photon response and multiplication of InSe/BP APDs (grey line, dark; red line, 4 μm laser illuminated with 30 μW and blue line, the corresponding multiplication factor). **(k)** $I_{ds}$–$V_{ds}$ curves at different temperatures (from 40 to 180 K). **(l)** Threshold voltages ($V_{th}$) of the avalanche breakdown and multiplication as functions of temperature. (a–c) Reproduced from Ref. [39]; (d–g) Reproduced from Ref. [41]; (h–l) Reproduced from Ref. [49].

form vertical heterojunctions, the periodic grating structures can effectively excite highly-confined plasmon waves in graphene and achieve $10^7$ A·W$^{-1}$ photoresponsivity at 6–16 μm wavelength. In conventional avalanches [Fig. 4(h)], the energy of the external electric field is absorbed by holes, which further impact the ionized atoms in a cascade manner, generating a great deal of free electrons and holes for fast current multiplication. Since avalanches occur randomly, a large amount of excess noise will exist. The ballistic avalanche process is shown in Fig. 4(i), under the action of the electric field, the hole accelerates and hits the A plane to produce one electron-hole pair. After the two holes are absorbed, the electron enters the electric field. The electron accelerates and hits plane B to produce a pair of electron-hole pairs. Due to the symmetric band structure of BP, electrons, and holes have almost equal ionization probabilities, and the absence of scattering allows ballistic avalanches to occur without introducing any excess white noise. To expand the application in the single-photon field of two-dimensional materials, Gao *et al.* [49] made vertical PN heterojunction by InSe/BP based on the principle of ballistic avalanche in Fig. 4(j), which maintained low power consumption and low noise while realizing carrier multiplication amplification. In conventional avalanches [Fig. 4(h)], the energy of the external electric field is absorbed by holes, which further impact the ionized atoms in a cascade manner, generating a great deal of free electrons and holes for fast current multiplication. Since avalanches occur randomly, a large amount of excess noise will exist. The ballistic avalanche process is shown in Fig. 4(i), under the action of the electric field, the hole accelerates and hits the A plane to produce one electron-hole pair. After the two holes are

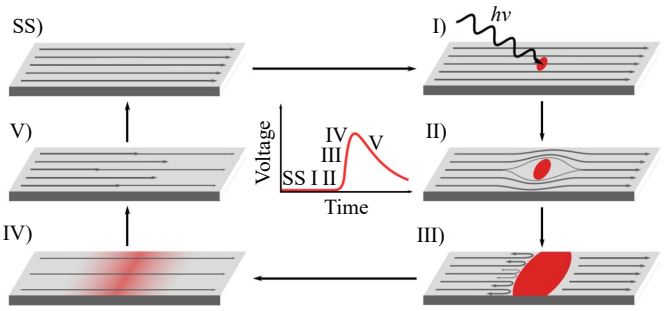


**Fig. 5** Single photon detection principle of superconducting nanowire. Reproduced from Ref. [56].

absorbed, the electron enters the electric field. The electron accelerates and hits plane B to produce a pair of electron-hole pairs. Due to the symmetric band structure of BP, electrons and holes have almost equal ionization probabilities, and the absence of scattering allows ballistic avalanche to occur without introducing any excess white noise. The mid-infrared detector based on this ballistic avalanche phenomenon exhibits a positive temperature coefficient (the current jump value in Fig. 4(k) barely changes from 40 to 180 K), extremely high photon amplification [greater than 10 000 in Fig. 4(l)] and noise performance below the theoretical limit of conventional avalanche photodetector.

## 2.2 Single-photon superconducting nanowire

### 2.2.1 Principle of single-photon detection superconducting nanowire

Single-photon superconducting nanowires is based on the superconducting Bardeen–Cooper–Schrieffer theory (BCS theory), which causes the state change of nanowires between the constant state and the superconducting state by absorbing photon energy from the nanowires, and the resulting gingal changes for photon detection. As shown in Fig. 5, the light irradiation will cause several Cooper electron pairs on the nanowire. The Cooper pair rotates in a certain area, forming a regional current. With the number of photons increasing, the current near the electron Cooper pair increases the critical current density beyond the superconducting nanowires. The nanowires change from a superconducting state to a constant resistance state and the detection system detects an electrical signal, then the nanowire returns to a superconducting state again.

Since superconducting nanowires are single-photon detection based on signal fluctuations generated by absorbing single or several electrons, their detection sensitivity and detection efficiency are very high, so SNSPD has become the leading technology equipment [14]. At present, the most widely used materials for superconducting nanowire single-photon detectors are niobium nitride (NbN [50, 51]) and Niobium nitride titanium (NbTiN [52]) because of their high superconducting transition temperature ($T_C$ = 1–6 K) and fast thermal recovery time [53]. Advanced materials such as NbN can achieve detection efficiency close to 100%, and the change time of constant state and superconducting state is fast, so SNSPD has a fast reset time, the low temperature decides the low dark count rate and low time jitter. However, its shortcomings are also obvious, subject to the superconducting transition temperature and the preparation process of superconducting nanowires, the current detection working temperature still does not exceed 100 K, and the line width is also limited to the nanometer range, although some literature reports the work of superconducting microwires, it always needs extremely low temperature. The width of nanowires is generally less than 120 nm, and some recent studies have reported that superconducting micro-strip single-photon detectors have a larger critical current density and lower dynamic sense than superconducting nanowire single-photon detectors, making them more suitable for manufacturing large-area detectors [54]. Ejrnaes *et al.* [55] reported the 4-nm-thick NbRe micro-strip with single-photon sensitivity as a single-photon detector at a temperature of 1.79 K and 1.5 μm band.

### 2.2.2 Superconducting nanowire materials-based single photon detection

Superconducting nanowires have a larger spectral response in the field of single photon detection than avalanche diodes. In addition, SNSPDs have developed rapidly in recent years, and the DE of SNSPD has reached more than 95% and close to 100%. In 2017, a research team [57] successfully realized SNSPD with a working wavelength of 1550 nm and a photon detection efficiency of more than 90% by using NbN ultra-thin film for the first time in the world. In 2019, another team developed SNSPD devices by replacing single nanowires with double nanowires on a dielectric mirror. The photon response rate and absorption efficiency were improved simultaneously. Korzh *et al.* [58] demonstrated that the NbN system has a temporal resolution of 2.6 ± 0.2 ps at visible wavelengths and 4.3 ± 0.2 ps at 1550 nm. Zhang *et al.* [59] adjusted the superconducting gap and Fermi level electron density of superconducting polycrystalline NbN ultrathin film through the helium ion irradiation defect project and found that with the increase of helium ion flux, the detection rate of the system significantly increased from 49% to 92%.

The future of single photon detection of superconducting nanowires will face the following challenges: (i) Increase the operating temperature of nanowire detection to reduce equipment and material costs. This requires the development of high-temperature superconducting materials with better performance. (ii) Manufacture larger

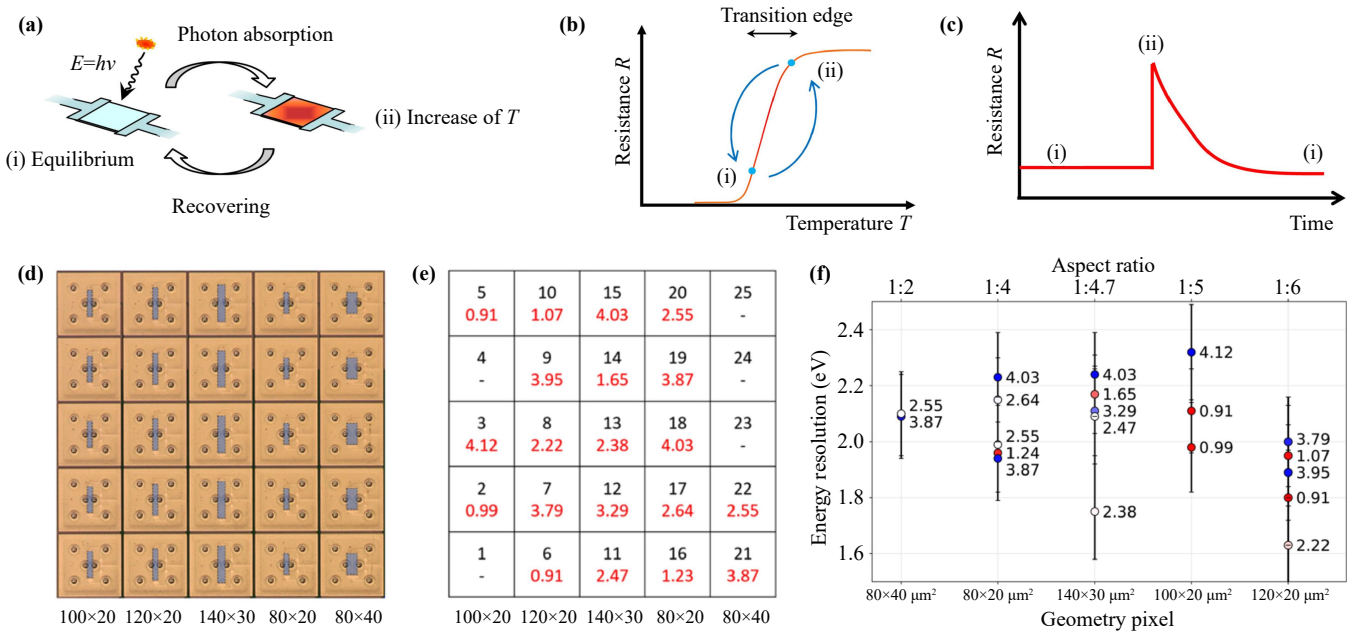


**Fig. 6** **(a)** TES Single photon detection schematic diagram. **(b)** The TES resistance changes near the superconducting transition temperature and. **(c)** TES resistance changes with photon absorption. **(d)** Microscope images of various sizes of Au-TES layouts on the chip. **(e)** Schematic layout of the TES array. The top number (black) indicates the TES number used. The bottom number, in red, gives the AC bias frequency in MHz for each TES. **(f)** Measured energy resolution for all geometries. (a–c) Reproduced from Ref. [60]; (d–f) Reproduced from Ref. [64].

superconducting nanowires at the centimeter scale or larger. (iii) The preparation of nanowire detection cameras with higher accuracy.

### 2.3 Superconducting transition edge sensor

Superconducting transition-edge sensor (TES) has extremely high detection sensitivity in the visible/near-infrared band. It can distinguish the number of photons, and the energy discrimination rate is very high in the X-ray and other high-energy bands. And the aforementioned semiconductive SPDs (Si-SPAD, InSb, HgCdTe, etc.), the superconducting TES detector has higher detection efficiency, faster response speed, lower dark count, and higher energy resolution. TES single-photon detector is a thermal detector consisting of a superconducting thin film and electrodes located at both ends of the film. As is illustrated in Fig. 6(a), when a photon of energy E is incident on the TES in an equilibrium state in the temperature transition region [Fig. 6(a)(i)], the temperature of the superconducting film is changed by absorption, the photon energy is slightly increased. The superconducting film rapidly switch from an equilibrium state to a normal state in the transition interval [Fig. 6(a)(ii)], and its resistance increases sharply. In Fig. 6(b), the resistance of TES film resistance is directly proportional to the absorbed photon energy ($\Delta E$) with the change of temperature. Therefore, the energy of absorbed photons can be inferred for the change of resistance on the time scale in Fig. 6(c). For single photon detection, TES is required to have high resistance sensitivity [60]. In a certain period, the absorbed energy is further dissipated from the TES film, and the temperature of the TES film returns to the original equilibrium state. The energy of the photon beam is proportional to the number of photons so for a fixed wavelength of incoming photons. The number of incident photons can be determined by the response waveform outputted by the detector [61]. The energy resolution ($\Delta E$) in the strong electro-thermal feedback is related to the heat capacity ($C$) of superconducting thin film. $\Delta E$ further characterizes the sensitivity of the detector. For the best $\Delta E$, the $C$ of the film should be as low as possible. High-energy resolution ($\Delta E$) is crucial for quantum-key distribution applications for TES. $\Delta E$ can be written as [62, 63]

$$\Delta E = 2\sqrt{2\ln 2}\sqrt{4k_{\mathrm{B}}T_0^2\frac{C}{\alpha_I}\sqrt{\frac{n\left(1+2\beta_I\right)}{2}}}, \tag{1}$$

where $k_{\mathrm{B}}$ is the Boltzmann constant, $n$ is the material-dependent exponent for the thermal conductivity, $T_0$ is the electron temperature, $\alpha_I$ is the temperature sensitivity, and $\beta_I$ is the current sensitivity.

The principle of TES is related to resistance, so the size and thickness of the superconducting film are related to the detection efficiency. As shown in Figs. 6(d, e), de Wit *et al.* [64] proves that the high aspect ratio for TES will prefer the critical temperature

**Table 1** Performance information of different single-photon detectors.

| Detector type | Working parameter (wavelength, time jitter/tj) | Performance (detection range, depth resolution, etc.) | Year | Ref. |
|---|---|---|---|---|
| PMTs | 200–1100, 1550 nm | 2–40 QE at 200–300 K | – | [78] |
| Ge-APD | 1310 nm | DE:5.27%, dark count rate of 534 kHz at 80 K | 2017 | [79] |
| Si-SPAD | 400–1000 nm | 50%–92% QE at 200–300 K | – | [80, 81] |
| InGaAs/InAlAs-SPAD | 1310 nm | 61.2% DE at 200 K | 2022 | [82] |
| InGaAs/InAlAs-SPAD | 1550 nm, 53 ps tj | sensitivities of –57.2 dBm, –53.42 dBm, and –51.06 dBm at bit rates of 100 Mbit/s, 200 Mbit/s, and 400 Mbit/s | 2022 | [25] |
| InGaAs/InAlAs-SPAD | 50 keV X-ray | 4.1 Mcps at 50 keV, NEP/$P_s$ ($2.5 \times 10^{-15}$ W·μm$^2$/Hz$^{3/2}$) | 2023 | [83] |
| NbRe-SMSPD | 1.5 μm | — | 2022 | [55] |
| NbN SMSPD | 1550 nm.48 ps tj | 92.2% SDE, 200 cps DCR, at 0.84 K | 2021 | [54] |
| NbN-SNSPD | 1550 nm | 92%SDE at 2.2 K | 2019 | [59] |
| WSi-SNSPD | 1520–1610 nm, 150 ps tj, 1cps DCR | 93% SDE at 2 K | 2013 | [84] |
| NbN-SNSPD | visible wavelengths and 1550 nm | 2.6 ± 0.2 ps system temporal resolution (STR) for visible wavelengths , 4.3 ± 0.2 ps STR at 1550 nm | 2020 | [58] |
| MoSi-SNSPD | 1542 nm, 76ps tj | 87.1%±0.5% SDE for 1542 nm at 0.7 K | 2015 | [85] |
| MoSi-SNSPD | 1550 nm | 98.0%±0.5% SDE for 1550 nm, | 2020 | [86] |
| NbTiN-SNSPD | 1260–1625 nm, 15–26ps tj | 99.5% SDE for 1350 nm, | 2022 | [87] |
| MoSi-SNSPD | 1550 nm, 15ps tj | full-width at half-maximum values of 4.8 ps for 532 nm and 10.3 ps for 1550 nm single photons, lowest temporal jitter of 15 ps | 2018 | [88] |
| Bi-TES | 10 keV and 15.6 keV X-ray | 40.3% and 30.7% absorptivity | 2016 | [65] |
| TiAu-TES | 5.9 keV X-ray | 2.4 eV energy resolution for 140 × 30 μm$^2$ at 110 mK | 2020 | [67] |
| TiAu-TES | 5.9 keV X-ray | 1.75 ± 0.10 eV energy resolution for 50 × 50 μm$^2$ ($T_c$ = 80.77 ± 0.70 mK) | 2022 | [89] |
| TiAu-TES | 1550 nm | 0.067 eV energy resolution for 8 × 8 μm$^2$ at 115 mK | 2022 | [75] |
| Ti/Au -TES | 1550 nm | 0.19 eV energy resolution for 20 × 20 μm$^2$ at 46 mK | 2022 | [90] |
| BLG-$MoS_2$ | 470–700 nm | 2%–4% at 100 K | 2018 | [47] |

(90 mK), and achieve excellent energy resolution with an array average of 2.03 ± 0.17 eV at 5.9 keV and a best-achieved resolution of 1.63 ± 0.17 eV as shown in Fig. 6(f). At present, superconducting films, such as tantalum (Ta) [65], semimetal (Bi) [66], gold (Au) [67], and titanium (Ti) [68–70], have been used as TES thin films for single photon remote detection [71]. Compared to superconducting nanowires, transition-edge sensors (TES) offer higher sensitivity, making them suitable for single-photon detection in the terahertz band. However, since TES utilizes the principle of thermal effect, the reaction time is slow, and further development is still needed in the field of quantum communication. The TES single photon detector wave has good detection efficiency in the terahertz to gamma-ray band [72, 73].

In 1998, the first superconducting TES single photon detector was developed, consisting of a TES film with W. It had a critical temperature ($T_c$) of 80 mK, a size of 18 μm$^2$, and a recovery time of 60 μs [74]. At present, the best energy resolution that a superconducting TES single-photon detector can achieved is 0.067 eV [75]. Through the integrated optical resonator, the superconducting TES single-photon detector has been able to absorb nearly 100% at multiple bands such as 850 nm [76] and 1550 nm [77], and the combined single photon resolution of multiple detectors will be further improved. de Wit *et al.* [64] found that the critical temperature has a dependence on the dimensions of the devices and the thermal conductance scales with the TES perimeter. The energy resolution and response speed of the superconducting TES single photon detector are affected by the superconducting transition temperature $T_c$, the lower the $T_c$, the higher the energy resolution, while the response speed will also be slower. The response speed is determined by the process in which the TES film resistance recovers from the normal state peak to the superconducting state. A faster recovery leads to a faster response speed for the detector. Until now, two main methods are used to improve the response speed increasing the thermal sensitivity parameters and increasing the critical temper-

ature of the film. Since most TES-absorbed layers are metal, reflection will inevitably occur on the metal surface, so the absorption efficiency of photons is significantly related to the detection efficiency of single photons and places an important limitation on the device's performance. At present, optical absorption cavity and waveguide integration are widely used in TES single-photon detection [76]. Therefore, the next method is to further explore how to improve the response speed of the device while maintaining high resolution.

### 2.4 Other single photon detections

#### 2.4.1 Photomultiplier tubes

The photomultiplier tubes (PMTs) are composed of a vacuum tube, a photocathode, a focusing electrode, and an electron multiplier tube. The light entering the photomultiplier tube is emitted into the vacuum tube, accelerated and focused by the focusing electrode, and impinges on the emission multiplier. Secondary electron emission occurs at each node of the electron multiplier, generating secondary electrons exponentially. Finally, the photoelectrons are extracted from the anode through multistage amplification. Although PMTs have a large active area, they are always subject to high operating voltages (in the kV range), low efficiency, and high DCR. Therefore, the field of SPDs is gradually being replaced by SPAD.

#### 2.4.2 Hybrid lead halide perovskite

In the field of medical imaging, semiconductor materials (such as Si [91], CdTe [92, 93], and CdZnTe [94]) were first proved to have single-photon sensitivity in X-ray medical imaging. Si and α-Se possess low stopping power for X-rays, making them suitable for portable X-ray fluorescence spectrometry focused on soft X-ray detection. However, this characteristic limits their potential application in the high-energy range beyond 50 keV [91]. Later, hybrid lead halide perovskite (HLHP) began to develop rapidly and proved to have the same properties, and hybrid lead halide perovskite is easy to be absorbed by solution and has lower cost. There are two main strategies for X-ray detection: direct type (using scintillators to convert X-ray photons into low-energy photons) [95] and indirect type (directly converts X-ray photons into electrical signals) [96].

X-ray imaging systems rely primarily on scintillators [97], which function by absorbing X-ray photons and then converting them into visible photons. These photons are then detected by photodiode arrays, which are often expensive and time-consuming to synthesize. For traditional perovskite X-ray detectors, self-absorption and lead toxicity are high, and the structural instability under high-pressure bias conditions and mixed electron-ion conductivity limits their application in high-end X-ray imaging. Lead halide perovskite X-ray scintillator detectors have demonstrated a low detection limit, rapid response speed, and superior spatial resolution up to the present time. Moreover, lead-free halide perovskites have also shown excellent scintillation properties. The X-ray detector prepared by Sakhatskyi *et al.* [98] using a solution prepared lead methyl iodide single crystal thin film has been proved to have single-photon sensitivity in zero-bias photovoltaic mode when 18 keV X-ray detection is adopted, the efficiency is as high as 88%, the noise equivalent power is 90 $pGy_{air}$, and the array sensor also has a high spatial resolution. Similar to X-ray imaging, gamma spectra can also be acquired by a combination of scintillators and pixel-scale sensitive photodetectors. For γ-ray detection of semiconductor materials put forward multiple stringent requirements, this is because the energy of γ-rays is much higher than that of X-rays, so it requires the material to have a large atomic number ($Z$) to obtain a strong blocking force [99]. The band gap of CdZnTe material is greater than 1.6 eV, and the large atomic number ensures a large blocking capability, so the single-crystal CdZnTe detector has achieved an energy resolution of 0.5% at room temperature [100].

## 3 Single photon detection parameter

### 3.1 Detection efficiency

The main parameters of single photon detectors are detection efficiency (DE), dark count, system dead time, time jitter, and so on. Detection rate (DR): the signal-to-noise ratio generated per unit incident radiation power, which is equal to the square root of the detector area divided by the noise equivalent power, and is a parameter to measure the sensitivity of the device. The detection efficiency is composed of photon absorption efficiency, optical coupling efficiency, and intrinsic detection efficiency. During device operating, the photon first needs to reach the physical area of the device, and then the photon is absorbed by the material. This process is related to the design of the device structure (such as reflection, filling factor ($f$), and cavity). In recent years, various researchers have continued to optimize the detection efficiency of the detector through structural enhancement of the device and exploration of new and alternative materials.

### 3.2 Dark count rate

Another application indicator of detectors is the dark count rate (DCR), which mainly includes the intrinsic dark count rate and background dark count rate of the detector itself. The background dark count is derived

from the blackbody radiation of the system and the stray light of the outside world and is proportional to the detection efficiency. The intrinsic dark count is proportional to the bias current. In general experiments, the effect of intrinsic dark count on detection efficiency is reduced by reducing the bias current. It is worth noting that dark current ($I_{dark}$) exists even in the absence of ambient light.

### 3.3 Light responsiveness

Optical response capability includes optical response ($R$) and optical response time ($\tau$). Optical response capability is one of the important parameters of photoelectric detection. It describes the change of photocurrent caused by light per unit power, which can be calculated by the following equation:

$$R = \frac{I_{ph}}{P}, \tag{2}$$

where $I_{ph}$ represents the actual measured photocurrent minus the dark current, and $P$ is the effective power of illumination on the device, that is, the power density of the laser times the area of the device. Optical corresponding time ($\tau$) represents the required time for the photodetector to change from the final output of 10% to 90% and describes the parameters of how fast the device responds to the incident radiation.

### 3.4 Quantum efficiency

Quantum efficiency (QE) can be further divided into internal quantum efficiency (IQE) and external quantum efficiency (EQE). EQE refers to the ratio between the number of photons emitted by the device and the number of carriers injected. It includes photon absorption, carrier generation, recombination and transport. IQE reflects the overall luminous efficiency of the device and describes the parameters of the photoelectric conversion of the device. Internal quantum efficiency refers to the percentage of photon number radiated by exciton recombination inside the device to the number of injected carriers. It only includes the efficiency of photon absorption and carrier generation inside the device with not the process of photons reaching the device surface. Usually, the IDE is less than the EQE. And sometimes the QE will be greater than 1 due to the existence of gain inside the detector,

$$IQE = \frac{N_{pr}}{N_{ab}}, \tag{3}$$

$$EQE = \frac{N_{pr}}{N_{ill}}, \tag{4}$$

$$EQE = IQE \cdot \eta_{out}, \tag{5}$$

where $N_{pr}$ is the number of electrons produced by the detector per unit of time, $N_{ab}$ represents the number of photons absorbed by the detector per unit time, $N_{ill}$ represents the number of photons a detector is illuminated per unit time. IQE takes the loss (or grain) into account, so it is generally larger (smaller) than the EQE, and The EQE is equal to the IQE multiplied by the photo-coupling output efficiency $\eta_{out}$. The DE depends on the thickness of the contact layer, the reflectance of the photodetector surface, the refractive index, the extinction coefficient of the absorption layer, etc.

Quantum efficiency is a parameter that evaluates the photoelectric conversion ability of a detector to incident photons. The photon detection efficiency (PDE or DE) refers to the ratio of photons detected by the device to the incident photons, and the IDE is internal detection efficiency, which does not consider the loss of signal from the external environment of the detector. In addition to the photoelectric conversion performance of the device, it also considers the overall response ability of the detector, including time resolution, responsivity, and time jitter. In short, quantum efficiency is a component of the detection efficiency, specifically targeting the photon-to-electron conversion efficiency, while the detection efficiency covers the overall response ability of the detector to the signal.

### 3.5 Signal-to-noise ratio (SNR)

Signal-to-noise ratio (SNR) refers to the ratio of output signal to noise. The detection wavelength of a single-photon detector is usually easily affected by environmental factors, so a high SNR is crucial for single-photon detection.

### 3.6 Time resolution

The time resolution of the detector means that the detector can distinguish the shortest time interval between two pulse photon signals, which is crucial for probing that requires high accuracy time measurements. And it is usually expressed in terms of the FWHM of the electrical signal. The higher the temporal resolution, the more precise temporal information can be provided by the detector. The improvement of the temporal resolution usually depends on the optimization of the structure design, materials, and detecting principles.

### 3.7 Time jitter

Similar to the time resolution, the time jitter refers to the undesired deviation between the truly periodic signal and the ideal periodic signal, and for periodic optical signals, the time jitter is usually expressed as the time variation of the electrical output signal, which will improve with the increase of the bias voltage.

### 3.8 Response speed

The response speed generally refers to the transit time of photogenerated charge carriers, which is expressed as the rise and fall time in the photogenerated current, and the response speed of the detector is usually represented by the maximum value of the rise or fall time. The rise time usually refers to the time required to increase the responsiveness from 10% to 90%, and the fall time usually refers to the time required to decrease the responsiveness from 90% to 10% [101].

### 3.9 Other single photon detection indicators

Noise equivalent power (NEP) is a method of measuring the sensitivity of a photodetector or detector system, defined as the signal power given a signal-to-noise ratio of 1 in unit Hertz output bandwidth. In addition, the photo-conductance gain (G) describes the ratio of photodetector's output current and the current directly generated by the incident photon, namely the built-in current gain. Dynamic linear range (LDR, XLDR): Describes the degree to which the photodetector's output signal maintains a linear relationship with the input signal. Time resolution: device optical response time and corresponding circuit response time.

## 4 Methods of improving single photon detector performance

### 4.1 Designed optical microcavity structure

Currently, optical cavity structure and integrated optical waveguide structure are used to improve the single photon detection efficiency of SNSPD. Multiple nanowires in parallel and changing the width and filling factor of superconducting nanowires can effectively improve the signal amplitude. Dielectric mirror structures and double-layer cavity structures are widely used to improve optical absorption in low-dimensional materials [102, 103]. The distributed Bragg reflector mirror (DBR mirror) consists several pairs of two or more kinds of semiconductor or dielectric materials with different refractive indices that are interlaced to obtain a high reflectivity within a specific optical band. In general, the most commonly used type of DBR mirror is a quarter-wave mirror, where the thickness of each layer corresponds to a quarter of the desired wavelength. This arrangement maximizes reflectivity at the desired wavelength. Additionally, a greater difference in refractive index between the two materials results in higher reflection efficiency. The greater the refractive index difference between the two dielectric layers, the fewer layers are required to achieve the target refractive index.

Nanowires implanted into the optical cavity structure can significantly improve the efficiency of light absorption. As shown in Fig. 7(a), Xu *et al.* [104] demonstrated that the optical absorptivity of superconducting nanowires was dependent on the line width and the filling factor $f$ (the fill factor $f$ is equal to the line width divided by the space between the two lines) in an alternating arrangement of $SiO_2/Ta_2O_5$ Bragg optical cavity. And Fig. 7(b) shows that the larger the filling factor, the higher the light absorption. When the filling factor $f$ is 0.8, the absorption rate nearly can reach 97%. But due to the narrow spacing of the nanometer microstrip, the grating interference effect will occur when the wavelength is larger than the grating spacing, resulting in the absorption decrease in a specific wavelength range. In Fig. 7(b), the optical absorption decrease can be seen near 1350 and 1800 nm. Cooling can affect the dark count rate and thermal noise of SNSPD and SMSPD, thus affecting the DE. At lower temperatures, the thermal excitation of the detector is reduced, and the superconducting state will be hotter, and the recovery time of the superconducting state to the constant resistance state will be faster. Therefore, superconducting nanowires usually operate at extremely low temperatures. Since the IDE of the SMSPD can be improved by decreasing the temperature in Fig. 7(c). A maximum SDE of 92.2% at a DCR of 200 cps at a wavelength of 1550 nm and a ratio of less than 1.03 between the maximum and minimum SDE calculated by Fig. 7(d) [104]. In Fig. 7(e), Wang *et al.* [105] reported a multispectral superconducting nanowire single photon detector constructed using a thickness-modulated optical thin film stack. As illustrated in Fig. 7(f), in contrast to the simple quarter-wave (QW) stack optical film, this unique optical thin film structure provides a modulated reflective band for single-photon detection over a well-separated, multi-wavelength range. The fabricated detector in Fig. 4(g) shows four detection bands and system detection efficiencies (SDEs) of 76.2%, 76.9%, 81.3%, and 85.0% at wavelengths 505 nm, 610 nm, 1030 nm, and 1550 nm respectively. With the same approach, Das [106] expanded the wavelength detection range of superconducting nanowires by leveraging multiple Bragg reflection cavities, with double layers at 400 to 2500 nm (three layers at 400 to 3000 nm) absorbing more than 60% efficiently. Salvoni *et al.* [107] optimized the scattering and absorption loss of photons in the system through all-dielectric laminated and fiber-coupled superconducting nanowires, achieving a system detection rate of 98%. The light absorption of two-dimensional material placed in the microcavity can be greatly improved [107]. SNSPDs made from 4.1 nm MoSi on the DBR (13 layers of α-Si/$SiO_2$) showed 98% SDE at 1550 nm (0.7 K) [107]. Therefore, achieving high SDE was facilitated by employing amorphous MoSi with robust saturated internal efficiency, utilizing optimized DBR, and incorporating fiber spacers. However, larger SNSPDs tend to cause high kinetic inductance, slower recovery, low yield, and higher jitter. This is notable for

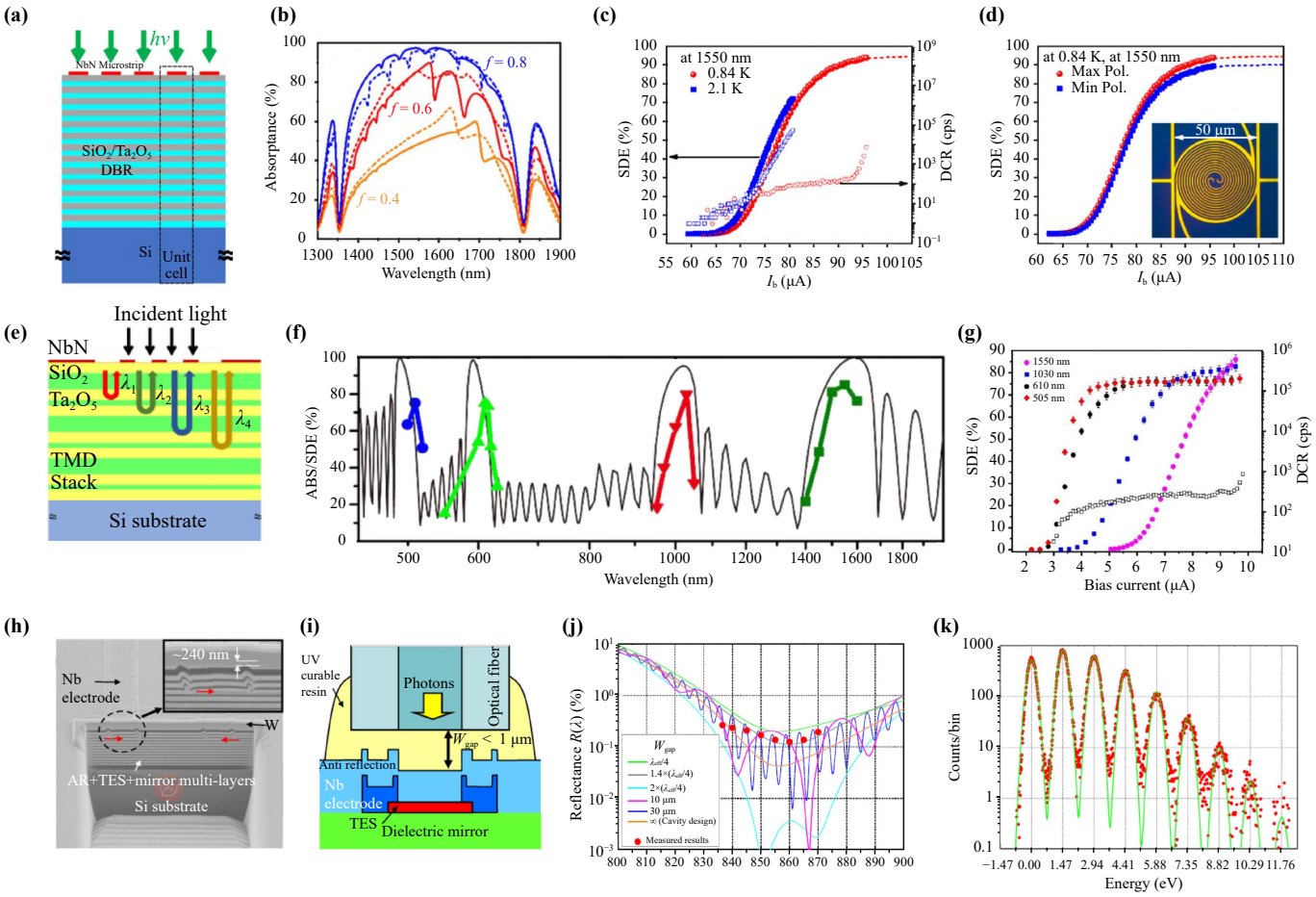


**Fig. 7** **(a)** Schematic cross-section of the NbN SMSPD with 13 layers of $SiO_2/Ta_2O_5$ Bragg mirror. **(b)** The relationship between different filling values $f$ on wavelength absorption. **(c)** The relationship between the bias current of the SMSPD on the SDE and DCR of SMSPD under 1550 nm illumination at 0.84 and 2.1 K. **(d)** The maximum and minimum SDE under different polarized lights (the dotted line is the function fitting, and the inset is the microscope image with an effective area of 50 μm). **(e)** Multispectral SNSPD schemata based on thickness-modulated $SiO_2/Ta_2O_5$ optical films. **(f)** For multilayer thickness-modulated optical films, simulated absorption and measurement system detection efficiency (SDEs) in the vicinity of multi-wavelength range. **(g)** The system detection efficiency (SDE) at 505, 610, 1030 and 1550 nm, and the dark count rate (DCR) as a function of the bias current. **(h)** SEM image of a cross-section of an optical TES cavity. Inset is the contact between TES and Nb electrodes. **(i)** Cross-sectional diagram of the fiber coupling. **(j)** The relationship of reflectivity and wavelength for TES single-photon detectors (The solid line shows the simulation results and the circle is the measured reflectance). **(k)** The energy distribution of the number of probe pulses laser of Ti-TES. (a–d) Reproduced from Ref. [104]; (e–g) Reproduced from Ref. [105]; (h–k) Reproduced from Ref. [76].

NbTiN-based large detectors, as the poly-crystalline nature of the materials often results in degradations of the performance due to higher film inhomogeneity compared to amorphous materials. A thicker Bragg reflector results in high light reflection and requires a larger detector to get good optical absorption. This results in high motion, long recovery time, and high-time jitter. Chang *et al.* [87] used a thinner $SiO_2$/Au membrane cavity obtaining an ultra-high reflective mirror with over 99% SDE at 1350 nm (also over 98% SDE at 1425 nm and Low time jitter (15–26 ps).

Both superconducting nanowires and special optical cavity structures are widely used in TES and other fields. Geng *et al.* [108] used an antireflection coating on the TES device fabricated on a dielectric mirror. They discovered that the performance of the Ti-based superconducting TES detector integrated into the 1550 nm optical cavity is twice that of the absorption rate without the integrated optical cavity [108]. Xu *et al.* [90] used inductively coupled plasma-assisted plasma-enhanced chemical vapor deposition (ICP-PECVD) to prepare $SiO_2$ and $SiN_x$ layers, coupled with fiber to reduce light wave reflection efficiency. The energy resolution of TES bilayer films (Ti/Au) can reach 0.19 eV, and discriminate up to 36 photon states. This special optical structure is also used in other materials, such as two-dimensional material photoelectric detection. However, the develop-

ment of weak light detection for two-dimensional materials has been restricted by weak light absorption for their atomic thickness. The optical cavity structure expands the application of two-dimensional materials in the field of low-light detection. Fukuda *et al.* [76] constructed a multilayer reflective optical cavity structure by magnetron sputtering multilayer dielectric films on titanium as seen in Figs. 7(h, i), and then coupled it with optical fiber to improve the optical absorption rate [Fig. 7(i)]. At the wavelength of 844 nm and 853 nm, the overall detection efficiency was determined to be 98±1%, reflecting a good single-photon detection ability [Fig. 7(j)]. Ti-TES detects pulse photons and finds that it is energy dependent. With the increase of photon energy, the photon counting rate decreases in Fig. 7(k). This is due to the fact that the higher the photon energy, the easier it is to achieve saturation and TES will output the signal after the photon energy reaches saturation.

### 4.2 Waveguide integration

The waveguide serves to confine energy within the waveguide medium, thereby minimizing energy loss during high-frequency and long-distance transmission processes. The waveguide can be compared to a kind of transmission line, where the important parameter of the waveguide transmission is the cut-off frequency ($f_c$). Only the energy higher than the $f_c$ can be transmitted in the waveguide, and the energy lower than the $f_c$ will be quickly attenuated in the transmission process, and the $f_c$ depends on the dimension of the waveguide cross-section. As a result, waveguide can be regarded as a high-pass filter. Waveguide integration is another widely used method to improve light absorption and increase detection efficiency. Waveguides can be mainly divided into the following categories: (i) Rectangular waveguide. This is the most common type of waveguide and is mainly used in the microwave frequency band. Its $f_c$ depends on its maximum side length. (ii) Circular waveguides. These waveguides are mainly used in high-frequency applications such as radar and satellite communications. Its $f_c$ depends on its diameter. (iii) Stripline waveguides. These waveguides are mainly used in low-frequency applications, such as television and broadcasting. Its $f_c$ depends on its width. (iv) Fiber waveguide. This kind of waveguide is mainly used for optical communication. Its $f_c$ depends on the diameter and refractive index of its fiber. (v) Surface waveguides. These waveguides are mainly used in UHF applications such as radar and satellite communications. Its $f_c$ depends on the properties of its surface. The light absorption is enhanced by increasing the interaction distance with the evanescent wave propagating along the waveguide, and the nanowires are prepared along the direction of the optical waveguide to facilitate prolonged interaction between light and nanowires, thereby improving light absorption capability. Ge [109], Si (ultra-compact size and low energy consumption) [110–113], $Si_3N_4$ (0.1 dB/cm low propagation loss and 400 nm to 2.35 μm wide transparency window) [114–116], InGaAs/InP [117], polymer [118–121] and many materials have been widely used in the field of waveguide integrated short- and long-reach optical interconnects. Wang *et al.* [124] proposed and fabricated a high-performance waveguide coupled SPAD with three electrical terminals (separate-absorption-charge), as depicted in Fig. 8(a), where the incident light is transmitted from the channel Si waveguide to the Ge absorption region through the grating coupler. By adjusting the electric field in the Ge absorption layer, DCR can be well reduced [Fig. 8(b)] without affecting the SPDE [Fig. 8(c)], but the weak electric field may prohibit the carrier to drift at the saturation speed in the Ge absorption layer. Thus, Fig. 8(d) exhibits a high time jitter when the bias voltage is small. In Fig. 8(e), Sahin *et al.* [122] proposed to use GaAs/$Al_{0.75}Ga_{0.25}$ As ridge waveguide to couple with NbN and found that the length of the waveguide was related to the absorption rate [Fig. 8(f)], and the quantum efficiency of the device in different modes could reach 24% at 1310 nm in Fig. 8(g), which had obvious photon-counting ability in Fig. 8(h) [122]. Gerrits *et al.* [123] demonstrated that tungsten is capable of photonic technology by constructing a waveguide-integrated TES in Fig. 8(i), compared to Fig. 8(k) without waveguide transient coupling, Fig. 8(j) clearly shows the separated pulse distribution, which proves that it has good photon resolution ability, and by optimizing the detector and adjusting the input polarization, the number of photons per pulse can reach 0.986 in TM mode. As shown in Fig. 8(l), it can be seen that the photon-number-resolving capability of the thin film is 10 μs [123].

In addition to the main single-photon detection mechanisms, some narrow band-gap 2D materials have recently achieved low-light detection in the communication band (O-L band) by coupling waveguides. For example, Wu *et al.* [125] integrated selenized $PdSe_2$ with silicon waveguide for on-chip photodetection with a high responsivity at 1260 to 1565 nm as shown in Fig. 9(a), which obtained low NEP of 4.0 pW·$Hz^{-0.5}$, and 3 DB bandwidth of 1.5 GHz measured data rate of 2.5 Gbit·$s^{-1}$. It can be seen from Fig. 9(b) that the electric field planed surface model simulated by TE indicates that the $PdSe_2$ coupled waveguide avoids high mode adaptation loss. A larger bias voltage exacerbates the generation-separation of photogenerated carriers, resulting in higher responsivity, therefore, different responsivity and external quantum efficiency are produced for the nanosheets with different thickness/length in Fig. 9(c). The waveguide coupled $PdSe_2$ photodetector can achieve broadband optical response, when the laser output power is fixed at different wavelengths, Due to the

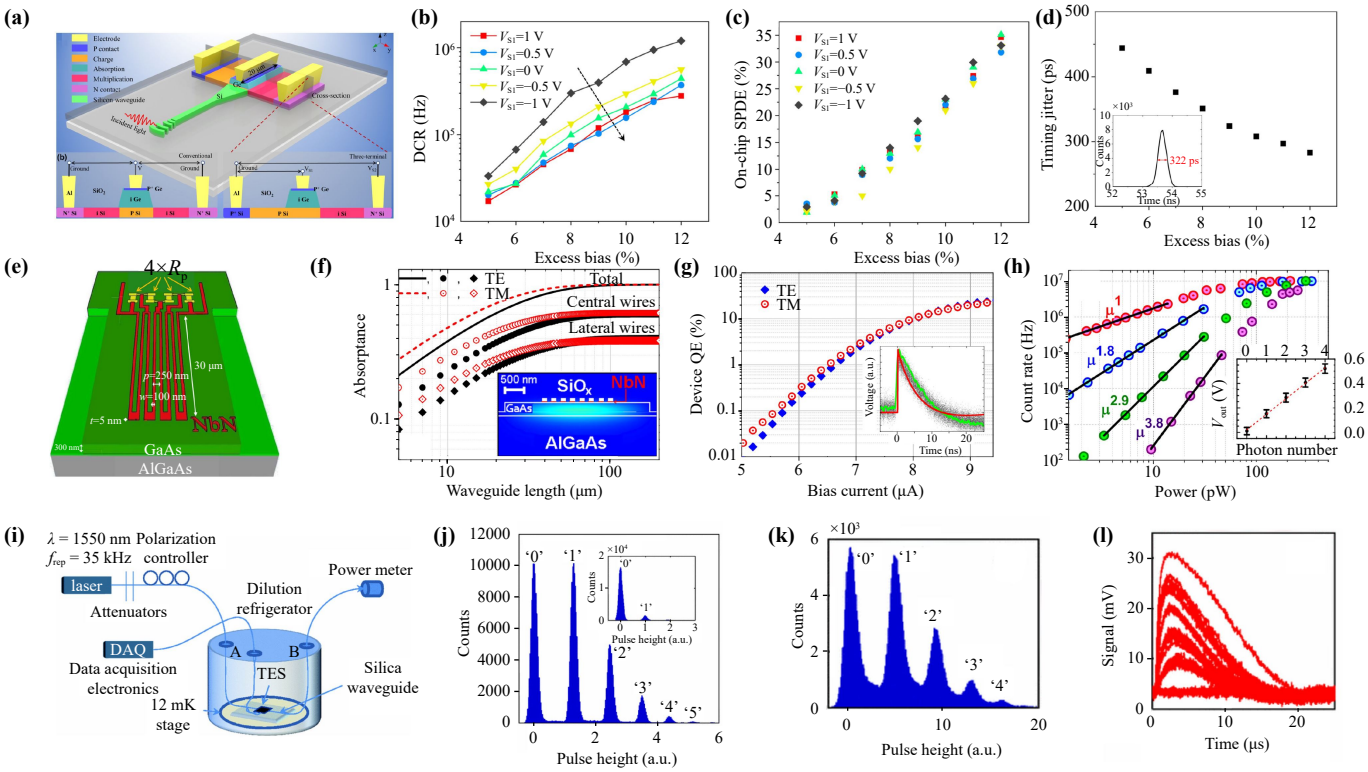


**Fig. 8** Waveguide integrated SPAD **(a)**, DCR **(b)** and SPDE **(c)** of the detection system versus the excess bias at 78 K. **(d)** The timing jitter as a function of excess bias at $V_{S1} = 1$ V where single-photon detection based on waveguide superconducting nanowires. **(e)** GaAs/$Al_{0.75}Ga_{0.25}As$ ridge waveguides based on NbN. **(f)** The calculated absorptivity in TE and TM modes, and the inset shows the electric field equivalent profile. **(g)** Device quantum efficiency (QE) at 1310 nm. **(h)** Photon count rate measured by pulsed laser at TE polarization at 1310 nm, $I_b = 8.8$ μA where waveguide integrated TES is used to single-photon detection. **(i)** Schematic of TES fabricated on optical waveguides at 1550 nm at 12 mK. The size of TES is 25 nm × 25 nm × 40 nm. **(j)** The photon pulse height distribution for the optimal TM polarization is plotted, and **(k)** the pulse height distribution without waveguide transient coupling. **(l)** The electrical TES output traces for different numbers of photons in the weak laser pulse. (a–d) Reproduced from Ref. [124]; (e–h) Reproduced from Ref. [122]; (i–k) Reproduced from Ref. [123].

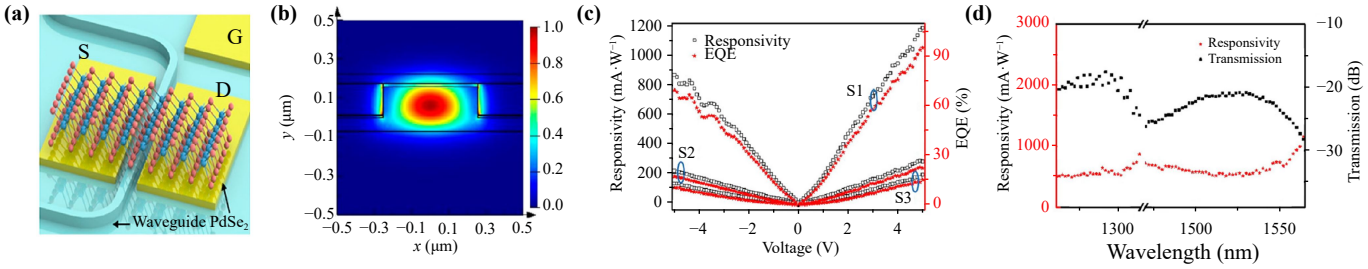


**Fig. 9** $PdSe_2$ photodetector integrated with silicon waveguide. **(a)** 3D illustration of the waveguide integrated $PdSe_2$ photodetector. **(b)** Calculated electric field profiles of the TE mode in the hybrid silicon/$PdSe_2$ waveguide. **(c)** Responsivity and EQE at different bias voltage at 1550 nm for different thickness/length $PdSe_2$ (S1 for 139 nm/22.6 μm, S2 for 142 nm/10.4 μm, S3 for 226 nm/14.7 μm). **(d)** Regulation of the gate voltage on the photon response (photocurrent and dark current), the optical power is 42 μW. Reproduced from Ref. [125].

different coupling efficiency of the grating couplers, the actual incident power at different wavelengths of the waveguide is also different. Smaller incident power usually brings a larger photocurrent gain and responsiveness (small incident optical power will cause less optical power loss, so the relative photocurrent gain is high). Therefore, the transmission and responsivity change in the opposite trend in Fig. 9(d). Similar to this kind of waveguide integrated narrow band gap two-dimensional materials suitable for communication bands also include BP [126, 127], $MoTe_2$ [128, 129], and $Bi_2O_2Se$ [130], and $PdSe_2$ [131].

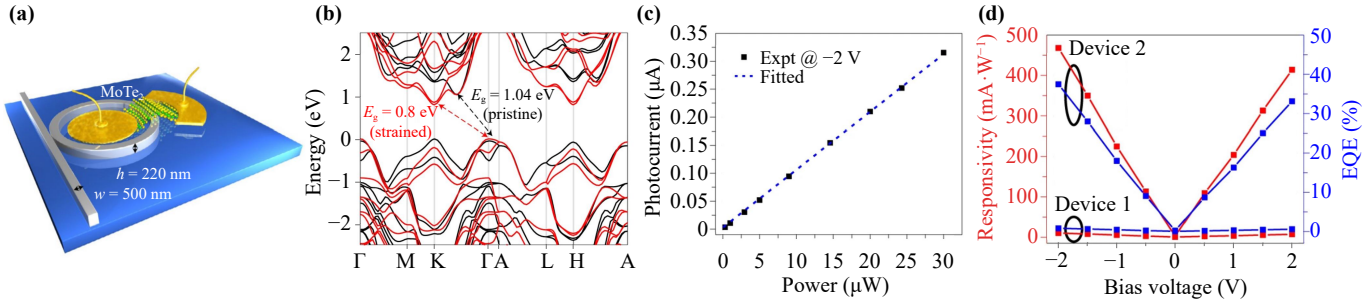


**Fig. 10** Strain-induced modulation of the electronic bandgap in $MoTe_2$. **(a)** Schematic diagram of MRR integrated $MoTe_2$ photodetector. **(b)** Bulk band structure DFT calculations of $MoTe_2$ before strain (black) and after 4% strain (red). **(c)** Photocurrent at different optical power. **(d)** The responsivity and EQE of the Au/$MoTe_2$/Au detector with different thickness/length (Device 1 for 40 nm/15 μm; Device 2 for 60 nm/30.7 μm). Reproduced from Ref. [152].

### 4.3 Strain engineering

Strain engineering is also a strategy capable of improving the light response, which is usually used to tune a material's properties by altering its mechanical or structural attributes [132–134] by modifying their atomic structure [135], lattice vibration [136], thermal conductivity, electrical and optical performance [135], and chemical activities [137]. By adjusting carrier concentration and other parameters, the band structure of a materials can be changed from direct band gap to indirect band gap and vice versa [138], and this method is widely used in two-dimensional materials. Due to the dimension of 2D materials, the reduction of surface defects, and the lack of interlayer slip, the Young's modulus and the strength of them are increased, so they can withstand greater stress than bulk materials [139, 140]. Strain engineering was originally used to open the conduction gap in graphene Dirac semi-metals in electronic device [141]. Strain engineering methods in 2D materials include substrate deformation induced strain [142–145], AFM tips [146–148], thermal expansion mismatches [149, 150], piezoelectric actuators [151], and controlled wrinkling. To apply strain to a two-dimensional material, it is usually used to transfer the material directly to an asymmetric or uneven surface, forming strain through mechanical bending of the two-dimensional material surface.

Induced strain can change the band structure of materials, which has a positive impact on the mobility of electrons. Therefore, the energy band gap of low-dimensional materials can be modulated by strain engineering, and high light response and low light detection can be achieved. For example, as shown in Fig. 10(a), Maiti *et al.* [152] fabricated a strain-induced $MoTe_2$ photodetector and integrated it with a silicon waveguide for photodetection at 1550 nm. In Fig. 10(c), it can be seen that the photocurrent changes linearly with the optical power to achieve a highly sensitive optical response and large EQE. The high responsiveness of $MoTe_2$ at 1550 nm is attributed to the reduction of the band gap caused by strain engineering [the band gap of the 2D material is reduced from 1.04 to 0.80 eV under strain induction, and the band gap modulation is 0.20 eV in Fig. 10(b)]. The enhancement of photon lifetime and absorption caused by integration with the non-planar waveguide and the performance of the device is affected by the ratio of thickness and length, the Au/$MoTe_2$/Au detector achieve nearly 1% and 37% EQE for Device 1 (for 40 nm/15 μm) and Device 2 (for 60 nm/30.7 μm), respectively in Fig. 10(d). Therefore, for single-photon detection, strain engineering is a cost-effective method to improve the optical responsivity and expand the detection wavelength, which is of great potential in the field of mid-far infrared detection in the future.

## 5 Application

### 5.1 Optical imaging

A photon is the smallest energy unit of light that can be detected. Traditional cameras realize object imaging by detecting light intensity at different positions, while single-photon imaging can reconstruct the image of the object by detecting the three-dimensional space position and time information of each photon [153]. For example in Fig. 11(a), researchers have used Si-SPAD arrays to achieve real-time 3D imaging of underwater targets [154]. Single-photon imaging counting can break through the signal-to-noise ratio limit of classical imaging, and effectively improve the working distance and quality of remote sensing and reconnaissance. In Fig. 11(b) the 3D image of an object hidden out of sight can be recovered by calculating the scattering and time-of-flight information of photons on the nearby wall, to identify and track the object out of sight [155]. SPAD combined with an imaging algorithm can realize the imaging of the target outside the scope of the camera field of view. This technology holds significant application value in fields such as anti-terrorism reconnaissance, medical detection, and beyond.

Traditional non-line-of-sight imaging (NLOS) is

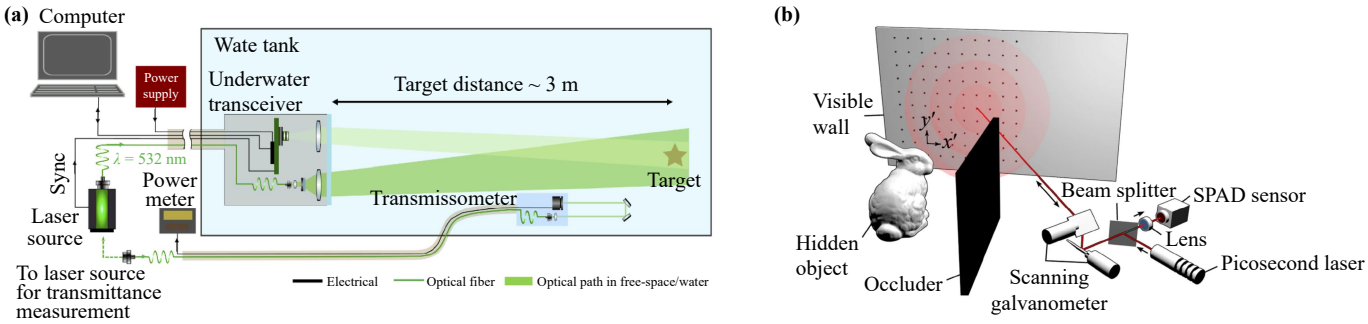


**Fig. 11** **(a)** Underwater imaging system for single-photon radar. Reproduced from Ref. [154]. **(b)** Non-view imaging. Reproduced from Ref. [5].

limited by the time resolution of SPAD (tens of picoseconds at best), and the imaging accuracy can only reach the centimeter level. It was reported that a near-infrared single-photon detector with a time resolution of 1.4 ps by using pulse pump frequency up-conversion detection technology [5], and reduced the dark count of the detector to 5 Hz through long-wave pumping and temporal filtering. On one hand, with the help of time-sharing detection of diffuse wall echo and target object signal echo, the NLOS system built by the single-photon detector effectively addresses the challenge of achieving a fully coaxial imaging system in NLOS scenarios. On the other hand, with the help of high temporal resolution, the high-precision 3D reconstruction of the out-of-view object is successfully realized, and the horizontal spatial resolution ability reaches 2 mm and the vertical spatial resolution ability reaches 0.18 mm. For avalanche diodes, the design process has also evolved from simple single-pixel to multi-pixel array imaging.

### 5.2 Biophotonics applications

In the field of biomedicine, antibody activity can be effectively obtained by fluorescent antibody labeling and single photon counting during antigen-antibody action. Biological protein molecules have good light absorption, energy transfer, and light emission [156]. Single-photon pulse-probe spectroscopy can be used to study the energy transfer of materials [157]. High-energy radiation based techniques such as X-ray detection are particularly important in many areas related to daily life. In advanced medical imaging, compared with the existing medical imaging modalities such as magnetic resonance imaging (MRI), computed tomography (CT), and cone beam computed tomography (CBCT), X-ray imaging is the most available and cheapest way. However, these medical imaging methods also have obvious disadvantages, such as radiation exposure, and high cost. Therefore, it is very important to improve the X-ray radiation dose and imaging quality. The basic principle of X-ray imaging is to record the attenuation of X-rays after they penetrate the human body and then image them. Small doses of X-rays penetrating living organisms can be applied in medical examinations, and penetrating non-living substances can be applied in product quality inspection [158], safety inspection, etc. As shown in Figs. 12(a–c), Jiang *et al.* [159] used a two-site doped perovskite single-crystal X-ray detector to achieve $(2.6 \pm 0.1) \times 10^4$ $\mu C \cdot Gy_{air}^{-1} \cdot cm^{-2}$ at a low field of 1 $V \cdot cm^{-1}$, with a state-of-the-art detectable dose rate of 7.09 $nGy_{air} \cdot S^{-1}$ and long-term stability of more than half a year. Sakhatskyi *et al.* [98] prepared single-crystal lead methyl iodide films with single-photon sensitivity by solution growth method as shown in Fig. 12(d) and demonstrated that 88% detection efficiency and noise-equivalent dose of 90 $pGy_{air}$ (18 keV X-ray) could be achieved in the photovoltaic mode under zero voltage bias [Fig. 12(e)] [98]. The energy resolution spectrum in Fig. 12(f) shows it has better performance in the field of X-ray two-color imaging.

### 5.3 Quantum communication

Lidar is used to study environmental parameters such as atmosphere, vegetation, and remote objects. Detector performance directly influences resolution, acquisition time, and maximum range in lidar systems. Single-photon ranging and detection both require single-photon sensitivity and picosecond timing resolution [160]. To achieve ultra-long distance high-precision 3D imaging, it is necessary to solve the strong noise in the echo process. As shown in Fig. 13(a), Li *et al.* [161] constructed an efficient and low-noise coaxial single-photon lidar system [Figs. 13(a) (iii)], and combined it with the remote algorithm to achieve single-photon 3D imaging as far as 45 km. It is of great significance for long-distance imaging and quantum communication. In the long-distance practical application of quantum secret key distribution (QKD), it is inevitable to have serious channel loss. The existing measurement-device-independent quantum key distribution (MDI-QKD) uses two-photon composite events as the effective detection events so that its secure code rate decreases linearly with the channel attenuation. Pan *et al.* [162, 163] have developed very low-noise

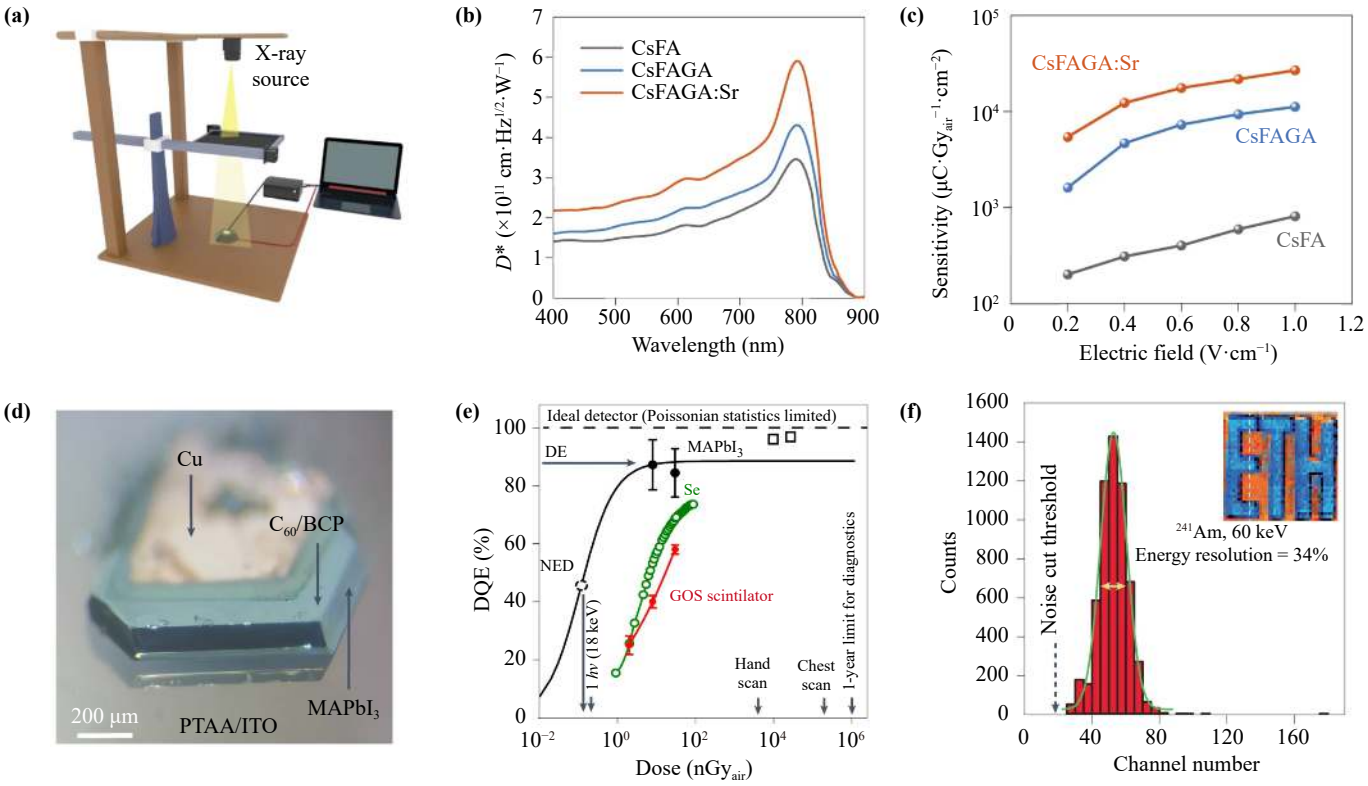


**Fig. 12** **(a)** Schematic of the X-ray imaging system. **(b)** Normalized response varying with the frequency. **(c)** Sensitivity of X-ray detectors under different electric fields. **(d)** $MAPbI_3$ SC XPV device and **(e)** DQE dependencies on the dose in γ-ray single-photon counting. The solid black line and points represent the model and experimental data. **(f)** Energy-resolved spectrum of 60 keV photons from a radioactive $^{241}Am$ source. The inset picture is Energy-resolved X-ray imaging of the object under 50 $kV_p$ X-ray irradiation. (a–c) Reproduced from Ref. [159]; (d–f) Reproduced from Ref. [98].

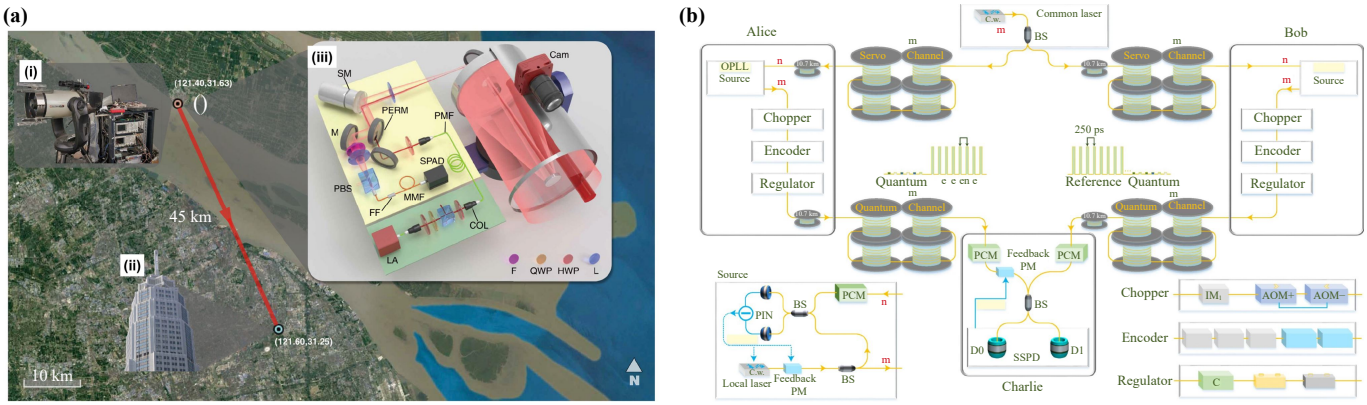


**Fig. 13** **(a)** Using single-photon laser radar (i), a high-rise building (ii) located 45 km away in Shanghai is imaged at a long distance. (iii) is the internal structure of single-photon lidar. **(b)** A single photon detector (SPD) was used to perform quantum key distribution on 830 km optical fiber. (a) Reproduced from Ref. [161]; (b) Reproduced from Ref. [164].

superconducting single-photon detectors. The dark count caused by thermal radiation is suppressed by multi-stage filtering in the 40 and 2.2 K temperature regions, and the noise of the single photon detector is reduced to 0.02 cps. Two-field quantum key distribution (TF-QKD) and phase-matched quantum key distribution (PM-QKD) of 500 km real environment fiber are realized. Guo *et al.* [164] used a superconducting NbN film single-photon detector to detect interference photons, which has a high detection efficiency and a low DCR. By changing the thickness of the film, Guo *et al.* [164] used an NbN-superconducting single-photon detector (NbN-SNSPD) to detect interference photons in Fig. 13(b), which a has high detection efficiency and a low DCR,

extending the secure transmission distance of optical fiber TF-QKD to more than 830 km and increased the secure code rate by 50–1000 times. Pan's group [29] reported coupling 1550 nm and 1950 nm signal photons through single-mode fiber coupling, using pigtailed periodically poled lithium niobate (PPLN) waveguide and Si-SPAD, the total detection efficiency reached 8% in 53-km ultra-long distance communication, the average dark count rate was 20 Hz, and the total channel loss was only 48 dB.

## 6 Conclusion

SPAD has become an indispensable basic technology in quantum communication, photon calculation, and precision measurement. In recent years, with the continuous development of optical technology and nanotechnology, SPAD has been widely developed and applied. PMTs, SPAD, SNSPD, TES, and HLHP are all shining in the field of single-photon detection from different detection mechanisms, different dimensions, different electric conductions, and different detection wavelengths. According to the dimension of the detector material, it can be divided into 0D quantum dots, 1D nanowires, 2D thin films, and 3D bulk materials. During the past decades, the synthesis of low-dimensional materials has gradually matured, which can effectively reduce the period loss, extend detection wavelengths, and achieve high-gain photon-counting detection by using the advantages of high mobility, atomic level thickness, and wide detection band combined with ballistic avalanche effect. Beyond that, low-dimensional materials are also gradually compatible with the CMOS technology. To increase the single-photon sensitivity, special optical cavities, and waveguide integration are used to improve the ability to couple with weak light. Multilayer cavity recombination or frequency up-conversion has been used to extend the detection wavelength. Although low-dimensional materials currently cannot replace traditional Si-SPAD and InGaAs/InP-SPAD, their special detection mechanisms (ballistic avalanche, photogating effect, etc.) have proven their potentials in photon counting. For photon-counting devices based on superconducting effects, such as SNSPD and TES, the superconductors should be as thin as possible to achieve low thermal capacity while ensuring performance as much as possible.

For single-photon detection, the main problem is how to separate the background noise and how to absorb the weak light. The former researchers have studied advanced efficient algorithms and optical fibers to reduce the noise in the process of light propagation. At present, the research on single-photon detection mainly focuses on special optical cavity structures, and waveguides are integrated to improve light absorption. Some low-dimensional materials with special band-gap use strain engineering to adjust the band-gap structure to improve optical sensitivity and extend the wavelength. Besides, the combination of SPAD with lidar technology, X-ray imaging, and efficient algorithms has realized mid-infrared imaging, long-distance imaging of nearly one thousand kilometers, low-loss quantum communication, low-radiation medical imaging, and non-view-field imaging. However, it is still challenging to further expand the detection range because the photon signal intensity decays quadratic function with the increase of distance, and the background noise is also affected by atmospheric scattering and operation. For example, the operating temperature of high-performance SNSPD is below 5 K. The development of single-photon detection technology requires not only high detection efficiency but also the combination of high-power lasers and efficient imaging algorithms to further improve the application practice.

**Declarations** The authors declare that they have no competing interests and there are no conflicts.

**Acknowledgements** This work was financially supported by the National Natural Science Foundation of China (Grant Nos. 52272160, U2330112, and 52002254), the Sichuan Science and Technology Foundation (Grant Nos. 2023YFSY0002, 2020YJ0262, 2021YFH0127, 2022YFH0083, and 2022YFSY0045), the Chunhui Plan of Ministry of Education of China, Fundamental Research Funds for the Central Universities, China (Grant No. YJ201893), and the Open-Foundation of Key Laboratory of Laser Device Technology, China North Industries Group Corporation Limited (Grant No. LLDT2023-006).

## References

1. Y. F. Yan, L. Zhou, W. Zhong, and Y. B. Sheng, Measurement-device-independent quantum key distribution of multiple degrees of freedom of a single photon, *Front. Phys.* 16(1), 11501 (2021)
2. J. P. Chen, C. Zhang, Y. Liu, C. Jiang, D. F. Zhao, W. J. Zhang, F. X. Chen, H. Li, L. X. You, Z. Wang, Y. Chen, X. B. Wang, Q. Zhang, and J. W. Pan, Quantum key distribution over 658 km fiber with distributed vibration sensing, *Phys. Rev. Lett.* 128(18), 180502 (2022)
3. Y. Ma, Y. Z. Ma, Z. Q. Zhou, C. F. Li, and G. C. Guo, One-hour coherent optical storage in an atomic frequency comb memory, *Nat. Commun.* 12(1), 2381 (2021)
4. M. Grein, A. Kerman, E. Dauler, M. Willis, B. Romkey, R. Molnar, B. Robinson, D. Murphy, and D. Boroson, An optical receiver for the Lunar Laser Communication Demonstration based on photon-counting superconducting nanowires, SPIE, Vol. 9492 CSI, 2015
5. B. Wang, M. Y. Zheng, J. J. Han, X. Huang, X. P. Xie, F. Xu, Q. Zhang, and J. W. Pan, Non-line-of-sight imaging with picosecond temporal resolution, *Phys. Rev. Lett.* 127(5), 053602 (2021)
6. Z. P. Li, J. T. Ye, X. Huang, P. Y. Jiang, Y. Cao, Y.

Hong, C. Yu, J. Zhang, Q. Zhang, C. Z. Peng, F. Xu, and J. W. Pan, Single-photon imaging over 200 km, *Optica* 8(3), 344 (2021)
7. W. He, Z. Feng, J. Lin, S. Shen, Q. Chen, G. Gu, B. Zhou, and P. Zhang, Adaptive depth imaging with single-photon detectors, *IEEE Photonics J.* 9(2), 7801812 (2017)
8. S. Scholes, G. Mora-Martín, F. Zhu, I. Gyongy, P. Soan, and J. Leach, Fundamental limits to depth imaging with single-photon detector array sensors, *Sci. Rep.* 13(1), 176 (2023)
9. Y. Wang, K. Huang, J. Fang, M. Yan, E. Wu, and H. Zeng, Mid-infrared single-pixel imaging at the single-photon level, *Nat. Commun.* 14(1), 1073 (2023)
10. K. Rajendran, M. Petersilka, A. Henning, E. R. Shanblatt, B. Schmidt, T. G. Flohr, A. Ferrero, F. Baffour, F. E. Diehn, L. Yu, P. Rajiah, J. G. Fletcher, S. Leng, and C. H. McCollough, First clinical photon-counting detector CT system: Technical evaluation, *Radiology* 303(1), 130 (2022)
11. A. S. Kowligy, H. Timmers, A. J. Lind, U. Elu, F. C. Cruz, P. G. Schunemann, J. Biegert, and S. A. Diddams, Infrared electric field sampled frequency comb spectroscopy, *Sci. Adv.* 5(6), eaaw8794 (2019)
12. I. Pupeza, M. Huber, M. Trubetskov, W. Schweinberger, S. A. Hussain, C. Hofer, K. Fritsch, M. Poetzlberger, L. Vamos, E. Fill, T. Amotchkina, K. V. Kepesidis, A. Apolonski, N. Karpowicz, V. Pervak, O. Pronin, F. Fleischmann, A. Azzeer, M. Žigman, and F. Krausz, Field-resolved infrared spectroscopy of biological systems, *Nature* 577(7788), 52 (2020)
13. C. Niclass, C. Favi, T. Kluter, F. Monnier, and E. Charbon, Single-photon synchronous detection, *IEEE J. Solid-State Circuits* 44(7), 1977 (2009)
14. B. Zhang, Y. Q. Guan, L. Xia, D. Dong, Q. Chen, C. Xu, C. Wu, H. Huang, L. Zhang, L. Kang, J. Chen, and P. Wu, An all-day lidar for detecting soft targets over 100 km based on superconducting nanowire single-photon detectors, *Supercond. Sci. Technol.* 34(3), 034005 (2021)
15. Q. Chen, R. Ge, L. Zhang, F. Li, B. Zhang, F. Jin, H. Han, Y. Dai, G. He, Y. Fei, X. Wang, H. Wang, X. Jia, Q. Zhao, X. Tu, L. Kang, J. Chen, and P. Wu, Mid-infrared single photon detector with superconductor $Mo_{0.8}Si_{0.2}$ nanowire, *Sci. Bull. (Beijing)* 66(10), 965 (2021)
16. F. T. Jaeckel, A. Roy, D. Wulf, S. Zhang, Y. Zhou, J. S. Adams, S. R. Bandler, J. A. Chervenak, A. M. Datesman, M. E. Eckart, A. J. Ewin, C. V. Ambarish, F. M. Finkbeiner, R. Kelley, C. A. Kilbourne, A. R. Miniussi, F. S. Porter, J. E. Sadleir, K. Sakai, S. J. Smith, N. Wakeham, E. Wassell, N. Christensen, W. Yoon, K. M. Morgan, D. R. Schmidt, D. S. Swetz, J. N. Ullom, R. Gruenke, L. Hu, D. McCammon, M. McPheron, M. Meyer, and K. L. Nelms, Energy calibration of high-resolution X-ray TES microcalorimeters with 3 eV optical photons, *IEEE Trans. Appl. Supercond.* 29(5), 1 (2019)
17. A. Incoronato, I. Cusini, K. Pasquinelli, and F. Zappa, Single-shot pulsed-LiDAR SPAD sensor with on-chip peak detection for background rejection, *IEEE J. Sel. Top. Quantum Electron.* 28, 3804210 (2022)
18. G. C. Shan, Z. Q. Yin, C. H. Shek, and W. Huang, Single photon sources with single semiconductor quantum dots, *Front. Phys.* 9(2), 170 (2014)
19. P. Martyniuk, P. Wang, A. Rogalski, Y. Gu, R. Jiang, F. Wang, and W. Hu, Infrared avalanche photodiodes from bulk to 2D materials, *Light Sci. Appl.* 12(1), 212 (2023)
20. A. Gallivanoni, I. Rech, and M. Ghioni, Progress in quenching circuits for single photon avalanche diodes, *IEEE Trans. Nucl. Sci.* 57, 3815 (2010)
21. A. Maccarone, G. Acconcia, U. Steinlehner, I. Labanca, D. Newborough, I. Rech, and G. S. Buller, Custom-technology single-photon avalanche diode linear detector array for underwater depth imaging, *Sensors (Basel)* 21(14), 4850 (2021)
22. H. Lee, H. Choi, and I. Yun, Junction engineering-based modeling and optimization of deep junction silicon single-photon avalanche diodes for device scaling, *IEEE Trans. Electron Dev.* 69(9), 4970 (2022)
23. M. Sanzaro, N. Calandri, A. Ruggeri, and A. Tosi, InGaAs/InP SPAD with monolithically integrated zinc-diffused resistor, *IEEE J. Quantum Electron.* 52(7), 1 (2016)
24. F. Telesca, F. Signorelli, and A. Tosi, Temperature-dependent photon detection efficiency model for InGaAs/InP SPADs, *Opt. Express* 30(3), 4504 (2022)
25. Y. Tian, Q. Li, W. Ding, D. Wu, Z. Lin, X. Feng, H. Zhang, X. Yu, and Y. Zhao, High speed and high sensitivity InGaAs/InAlAs single photon avalanche diodes for photon counting communication, *J. Lightwave Technol.* 40(15), 5245 (2022)
26. X. Meng, S. Xie, X. Zhou, N. Calandri, M. Sanzaro, A. Tosi, C. H. Tan, and J. S. Ng, InGaAs/InAlAs single photon avalanche diode for 1550 nm photons, *R. Soc. Open Sci.* 3(3), 150584 (2016)
27. J. Rothman, Physics and limitations of HgCdTe APDs: A review, *J. Electron. Mater.* 47(10), 5657 (2018)
28. R. H. Haitz, Model for the electrical behavior of a microplasma, *J. Appl. Phys.* 35(5), 1370 (1964)
29. S. K. Liao, H. L. Yong, C. Liu, G. L. Shentu, D. D. Li, J. Lin, H. Dai, S. Q. Zhao, B. Li, J. Y. Guan, W. Chen, Y. H. Gong, Y. Li, Z. H. Lin, G. S. Pan, J. S. Pelc, M. M. Fejer, W. Z. Zhang, W. Y. Liu, J. Yin, J. G. Ren, X. B. Wang, Q. Zhang, C. Z. Peng, and J. W. Pan, Long-distance free-space quantum key distribution in daylight towards inter-satellite communication, *Nat. Photonics* 11(8), 509 (2017)
30. M. T. Rakher, L. Ma, O. Slattery, X. Tang, and K. Srinivasan, Quantum transduction of telecommunications-band single photons from a quantum dot by frequency upconversion, *Nat. Photonics* 4(11), 786 (2010)
31. Y. S. Lee, Y. M. Liao, P. L. Wu, C. E. Chen, Y. J. Teng, Y. Y. Hung, and J. W. Shi, $In_{0.52}Al_{0.48}As$ based single photon avalanche diodes with stepped E-field in multiplication layers and high efficiency beyond 60%, *IEEE J. Sel. Top. Quantum Electron.* 28(2), 1 (2022)
32. D. Wu, J. Guo, C. Wang, X. Ren, Y. Chen, P. Lin, L. Zeng, Z. Shi, X. J. Li, C. X. Shan, and J. Jie, Ultra-

broadband and high-detectivity photodetector based on $WS_2$/Ge heterojunction through defect engineering and interface passivation, *ACS Nano* 15(6), 10119 (2021)

33. D. Wu, C. Guo, L. Zeng, X. Ren, Z. Shi, L. Wen, Q. Chen, M. Zhang, X. J. Li, C. X. Shan, and J. Jie, Phase-controlled van der Waals growth of wafer-scale 2D $MoTe_2$ layers for integrated high-sensitivity broadband infrared photodetection, *Light Sci. Appl.* 12(1), 5 (2023)
34. D. Wu, J. Guo, J. Du, C. Xia, L. Zeng, Y. Tian, Z. Shi, Y. Tian, X. J. Li, Y. H. Tsang, and J. Jie, Highly polarization-sensitive, broadband, self-powered photodetector based on graphene/$PdSe_2$/germanium heterojunction, *ACS Nano* 13(9), 9907 (2019)
35. L. Zeng, D. Wu, J. Jie, X. Ren, X. Hu, S. P. Lau, Y. Chai, and Y. H. Tsang, Van der Waals epitaxial growth of mosaic-like 2D platinum ditelluride layers for room-temperature mid-infrared photodetection up to 10.6 μm, *Adv. Mater.* 32(52), 2004412 (2020)
36. L. Zeng, W. Han, S. E. Wu, D. Wu, S. P. Lau, and Y. H. Tsang, Graphene/$PtSe_2$/pyramid Si van der Waals Schottky junction for room-temperature broadband infrared light detection, *IEEE Trans. Electron Dev.* 69(11), 6212 (2022)
37. S. Zeng, M. Zhao, F. Li, Z. Yang, H. Wu, C. Tan, Q. Sun, L. Yang, L. Lei, and Z. Wang, Crystalline orientation-tunable growth of hexagonal and tetragonal 2H-$PtSe_2$ single-crystal flakes, *Adv. Funct. Mater.* 34(6), 2308681 (2024)
38. L. Zeng, W. Han, X. Ren, X. Li, D. Wu, S. Liu, H. Wang, S. P. Lau, Y. H. Tsang, C. X. Shan, and J. Jie, Uncooled mid-infrared sensing enabled by chip-integrated low-temperature-grown 2D $PdTe_2$ Dirac semimetal, *Nano Lett.* 23(17), 8241 (2023)
39. M. Zavvari and V. Ahmadi, Self-quenched quantum dot avalanche photodetector for mid-infrared single photon detection, *Infrared Phys. Technol.* 62, 7 (2014)
40. E. J. Gansen, M. A. Rowe, M. B. Greene, D. Rosenberg, T. E. Harvey, M. Y. Su, R. H. Hadfield, S. W. Nam, and R. P. Mirin, Photon-number-discriminating detection using a quantum-dot, optically gated, field-effect transistor, *Nat. Photonics* 1(10), 585 (2007)
41. W. Luo, Q. Weng, M. Long, P. Wang, F. Gong, H. Fang, M. Luo, W. Wang, Z. Wang, D. Zheng, W. Hu, X. Chen, and W. Lu, Room-temperature single-photon detector based on single nanowire, *Nano Lett.* 18(9), 5439 (2018)
42. C. Tan, Z. Yang, H. Wu, Y. Yang, L. Yang, and Z. Wang, Electrically tunable interlayer recombination and tunneling behavior in $WSe_2$/$MoS_2$ heterostructure for broadband photodetector, *Nanoscale* 16(12), 6241 (2024)
43. Z. Ye, C. Tan, X. Huang, Y. Ouyang, L. Yang, Z. Wang, and M. Dong, Emerging $MoS_2$ wafer-scale technique for integrated circuits, *Nano-Micro Lett.* 15(1), 38 (2023)
44. C. Tan, R. Tao, Z. Yang, L. Yang, X. Huang, Y. Yang, F. Qi, and Z. Wang, Tune the photoresponse of monolayer $MoS_2$ by decorating $CsPbBr_3$ perovskite nanoparticles, *Chin. Chem. Lett.* 34(7), 107979 (2023)
45. O. Lopez-Sanchez, D. Lembke, M. Kayci, A. Radenovic, and A. Kis, Ultrasensitive photodetectors based on monolayer $MoS_2$, *Nat. Nanotechnol.* 8(7), 497 (2013)
46. Y. Zhang, T. Liu, B. Meng, X. Li, G. Liang, X. Hu, and Q. J. Wang, Broadband high photoresponse from pure monolayer graphene photodetector, *Nat. Commun.* 4(1), 1811 (2013)
47. K. Roy, T. Ahmed, H. Dubey, T. P. Sai, R. Kashid, S. Maliakal, K. Hsieh, S. Shamim, and A. Ghosh, Number-resolved single-photon detection with ultralow noise van der Waals hybrid, *Adv. Mater.* 30(2), 1704412 (2018)
48. Y. Liu, T. Gong, Y. Zheng, X. Wang, J. Xu, Q. Ai, J. Guo, W. Huang, S. Zhou, Z. Liu, Y. Lin, T. L. Ren, and B. Yu, Ultra-sensitive and plasmon-tunable graphene photodetectors for micro-spectrometry, *Nanoscale* 10(42), 20013 (2018)
49. A. Gao, J. Lai, Y. Wang, Z. Zhu, J. Zeng, G. Yu, N. Wang, W. Chen, T. Cao, W. Hu, D. Sun, X. Chen, F. Miao, Y. Shi, and X. Wang, Observation of ballistic avalanche phenomena in nanoscale vertical InSe/BP heterostructures, *Nat. Nanotechnol.* 14(3), 217 (2019)
50. R. Cheng, J. Wright, H. G. Xing, D. Jena, and H. X. Tang, Epitaxial niobium nitride superconducting nanowire single-photon detectors, *Appl. Phys. Lett.* 117(13), 132601 (2020)
51. P. Hu, H. Li, L. You, H. Wang, Y. Xiao, J. Huang, X. Yang, W. Zhang, Z. Wang, and X. Xie, Detecting single infrared photons toward optimal system detection efficiency, *Opt. Express* 28(24), 36884 (2020)
52. X. Yang, L. You, L. Zhang, C. Lv, H. Li, X. Liu, H. Zhou, and Z. Wang, Comparison of superconducting nanowire single-photon detectors made of NbTiN and NbN thin films, *IEEE Trans. Appl. Supercond.* 28(1), 2200106 (2018)
53. A. Vetter, S. Ferrari, P. Rath, R. Alaee, O. Kahl, V. Kovalyuk, S. Diewald, G. N. Goltsman, A. Korneev, C. Rockstuhl, and W. H. P. Pernice, Cavity-enhanced and ultrafast superconducting single-photon detectors, *Nano Lett.* 16(11), 7085 (2016)
54. G. Z. Xu, W. J. Zhang, L. X. You, J. M. Xiong, X. Q. Sun, H. Huang, X. Ou, Y. M. Pan, C. L. Lv, H. Li, Z. Wang, and X. M. Xie, Superconducting microstrip single-photon detector with system detection efficiency over 90% at 1550 nm, *Photon. Res.* 9(6), 958 (2021)
55. M. Ejrnaes, C. Cirillo, D. Salvoni, F. Chianese, C. Bruscino, P. Ercolano, A. Cassinese, C. Attanasio, G. P. Pepe, and L. Parlato, Single photon detection in NbRe superconducting microstrips, *Appl. Phys. Lett.* 121(26), 262601 (2022)
56. I. Esmaeil Zadeh, J. Chang, J. W. N. Los, S. Gyger, A. W. Elshaari, S. Steinhauer, S. N. Dorenbos, and V. Zwiller, Superconducting nanowire single-photon detectors: A perspective on evolution, state-of-the-art, future developments, and applications, *Appl. Phys. Lett.* 118(19), 190502 (2021)
57. W. Zhang, L. You, H. Li, J. Huang, C. Lv, L. Zhang, X. Liu, J. Wu, Z. Wang, and X. Xie, NbN superconducting nanowire single photon detector with efficiency over 90% at 1550 nm wavelength operational at compact

cryocooler temperature, *Sci. China Phys. Mech. Astron.* 60(12), 120314 (2017)

58. B. Korzh, Q. Y. Zhao, J. P. Allmaras, S. Frasca, T. M. Autry, E. A. Bersin, A. D. Beyer, R. M. Briggs, B. Bumble, M. Colangelo, G. M. Crouch, A. E. Dane, T. Gerrits, A. E. Lita, F. Marsili, G. Moody, C. Pena, E. Ramirez, J. D. Rezac, N. Sinclair, M. J. Stevens, A. E. Velasco, V. B. Verma, E. E. Wollman, S. Xie, D. Zhu, P. D. Hale, M. Spiropulu, K. L. Silverman, R. P. Mirin, S. W. Nam, A. G. Kozorezov, M. D. Shaw, and K. K. Berggren, Demonstration of sub-3 ps temporal resolution with a superconducting nanowire single-photon detector, *Nat. Photonics* 14(4), 250 (2020)
59. W. Zhang, Q. Jia, L. You, X. Ou, H. Huang, L. Zhang, H. Li, Z. Wang, and X. Xie, Saturating intrinsic detection efficiency of superconducting nanowire single-photon detectors via defect engineering, *Phys. Rev. Appl.* 12(4), 044040 (2019)
60. D. Fukuda, Single-photon measurement techniques with a superconducting transition edge sensor, in: *IEICE Transactions on Electronics* 2019, E102. C, pp 230–234
61. A. E. Lita, D. V. Reddy, V. B. Verma, R. P. Mirin, and S. W. Nam, Development of superconducting single-photon and photon-number resolving detectors for quantum applications, *J. Lightwave Technol.* 40(23), 7578 (2022)
62. K. Irwin and G. Hilton, Transition-edge sensors, in: Cryogenic Particle Detection, Berlin: Springer, 2005, pp 63–150
63. Y. Geng, P. Z. Li, J. Q. Zhong, W. Zhang, Z. Wang, W. Miao, Y. Ren, and S. C. Shi, Temperature and current sensitivity extraction of optical superconducting transition-edge sensors based on a two-fluid model, *Chin. Phys. B* 30(9), 098501 (2021)
64. M. de Wit, L. Gottardi, E. Taralli, K. Nagayoshi, M. L. Ridder, H. Akamatsu, M. P. Bruijn, M. D'Andrea, J. van der Kuur, K. Ravensberg, D. Vaccaro, S. Visser, J. R. Gao, and J. W. A. den Herder, High aspect ratio transition edge sensors for X-ray spectrometry, *J. Appl. Phys.* 128(22), 224501 (2020)
65. M. L. Ridder, P. Khosropanah, R. A. Hijmering, T. Suzuki, M. P. Bruijn, H. F. C. Hoevers, J. R. Gao, and M. R. Zuiddam, Fabrication of low-noise TES arrays for the SAFARI instrument on SPICA, *J. Low Temp. Phys.* 184(1–2), 60 (2016)
66. J. Chen, J. Li, X. Xu, Z. Wang, S. Guo, Z. Jiang, H. Gao, Q. Zhong, Y. Zhong, J. Zeng, and X. Wang, Electroplating deposition of bismuth absorbers for X-ray superconducting transition edge sensors, *Materials (Basel)* 14(23), 7169 (2021)
67. E. Taralli, L. Gottardi, K. Nagayoshi, M. Ridder, S. Visser, P. Khosropanah, H. Akamatsu, J. van der Kuur, M. Bruijn, and J. R. Gao, Characterization of high aspect-ratio TiAu TES X-ray microcalorimeter array under AC bias, *J. Low Temp. Phys.* 199(1-2), 80 (2020)
68. X. Xu, M. Rajteri, J. Li, S. Zhang, E. Monticone, J. Chen, C. Pepe, H. Gao, W. Li, X. Li, Q. Li, Y. Gao, Z. Liu, and X. Wang, Investigation of the superconducting Ti/PdAu bilayer films for transition edge sensors, *IEEE Trans. Appl. Supercond.* 32(4), 1 (2022)
69. X. Xu, J. Li, X. Wang, Q. Zhong, Y. Zhong, W. Cao, W. Li, J. Chen, Z. Zhao, Y. Gao, Z. Liu, and Q. He, in: 2020 Conference on Precision Electromagnetic Measurements (CPEM), pp 1–2
70. X. Xu, M. Rajteri, J. Li, S. Zhang, J. Chen, E. Monticone, Q. Zhong, H. Gao, W. Li, X. Li, Q. Li, Y. Zhong, W. Cao, S. Wang, Y. Gao, Z. Liu, and X. Wang, Influence of the interface composition to the superconductivity of Ti/PdAu films, *Nanomaterials (Basel)* 11(1), 39 (2020)
71. F. Shirazi, E. Gau, M. A. Hossen, D. Becker, D. Schmidt, D. Swetz, D. Bennett, D. Braun, F. Kislat, J. Gard, J. Mates, J. Weber, N. Rodriguez Cavero, S. Chun, L. Lisalda, A. West, B. Dev, F. Ferrer, R. Bose, J. Ullom, and H. Krawczynski, 511-CAM mission: A pointed 511 keV gamma-ray telescope with a focal plane detector made of stacked transition edge sensor microcalorimeter arrays, *J. Astron. Telesc. Instrum. Syst.* 9(2), 024006 (2023)
72. T. Kikuchi, G. Fujii, R. Hayakawa, R. Smith, F. Hirayama, Y. Sato, S. Kohjiro, M. Ukibe, M. Ohno, A. Sato, and H. Yamamori, Gamma-ray transition edge sensor with a thick $SiO_2/Si_xN_y/SiO_2$ membrane, *Appl. Phys. Lett.* 119(22), 222602 (2021)
73. M. Ohno, T. Irimatsugawa, H Takahashi, C Otani, T Yasumune, K Takasaki, C. Ito, T. Ohnishi, S. -I. Koyama, S. Hatakeyama, and R. M. T. Damayanthi, Superconducting transition edge sensor for gamma-ray spectroscopy, in: *IEICE Transactions on Electronics* 2017, E100. C, pp 283–290
74. B. Cabrera, R. M. Clarke, P. Colling, A. J. Miller, S. Nam, and R. W. Romani, Detection of single infrared, optical, and ultraviolet photons using superconducting transition edge sensors, *Appl. Phys. Lett.* 73(6), 735 (1998)
75. K. Hattori, T. Konno, Y. Miura, S. Takasu, and D. Fukuda, An optical transition-edge sensor with high energy resolution, *Supercond. Sci. Technol.* 35(9), 095002 (2022)
76. D. Fukuda, G. Fujii, T. Numata, K. Amemiya, A. Yoshizawa, H. Tsuchida, H. Fujino, H. Ishii, T. Itatani, S. Inoue, and T. Zama, Titanium-based transition-edge photon number resolving detector with 98% detection efficiency with index-matched small-gap fiber coupling, *Opt. Express* 19(2), 870 (2011)
77. A. E. Lita, A. J. Miller, and S. W. Nam, Counting near-infrared single-photons with 95% efficiency, *Opt. Express* 16(5), 3032 (2008)
78. Z. Deng, L. Ling, Y. Deng, C. Han, L. Yu, G. Cao, and Y. Wang, A novel visible light communication system prototype based on SiPM receiver, in: Proceedings of the 4th International Conference on Telecommunications and Communication Engineering, 2019
79. N. J. D. Martinez, M. Gehl, C. T. Derose, A. L. Starbuck, A. T. Pomerene, A. L. Lentine, D. C. Trotter, and P. S. Davids, Single photon detection in a waveguide-coupled Ge-on-Si lateral avalanche photodiode, *Opt. Express* 25(14), 16130 (2017)
80. D. A. Kalashnikov, S. H. Tan, M. V. Chekhova, and L. A. Krivitsky, Accessing photon bunching with a

photon number resolving multi-pixel detector, *Opt. Express* 19(10), 9352 (2011)
81. M. Ghioni, A. Gulinatti, I. Rech, F. Zappa, and S. Cova, Progress in silicon single-photon avalanche diodes, *IEEE J. Sel. Top. Quantum Electron.* 13(4), 852 (2007)
82. Y. S. Lee, Y. M. Liao, P. L. Wu, C. E. Chen, Y. J. Teng, Y. Y. Hung, and J. W. Shi, $In_{0.52}Al_{0.48}As$ based single photon avalanche diodes with stepped E-field in multiplication layers and high efficiency beyond 60%, *IEEE J. Selected Topics Quantum Electron.* 28(2), 3802107 (2022)
83. W. Ding, X. Feng, Y. Tian, Q. Li, X. Yu, Z. Lin, H. Zhang, X. Zeng, and Y. Zhao, InGaAs/InAlAs single photon avalanche photodiodes for X-ray detection, *IEEE Sens. J.* 23(18), 21254 (2023)
84. F. Marsili, V. B. Verma, J. A. Stern, S. Harrington, A. E. Lita, T. Gerrits, I. Vayshenker, B. Baek, M. D. Shaw, R. P. Mirin, and S. W. Nam, Detecting single infrared photons with 93% system efficiency, *Nat. Photonics* 7(3), 210 (2013)
85. V. B. Verma, B. Korzh, F. Bussières, R. D. Horansky, S. D. Dyer, A. E. Lita, I. Vayshenker, F. Marsili, M. D. Shaw, H. Zbinden, R. P. Mirin, and S. W. Nam, High-efficiency superconducting nanowire single-photon detectors fabricated from MoSi thin-films, *Opt. Express* 23(26), 33792 (2015)
86. D. V. Reddy, R. R. Nerem, S. W. Nam, R. P. Mirin, and V. B. Verma, Superconducting nanowire single-photon detectors with 98% system detection efficiency at 1550 nm, *Optica* 7(12), 1649 (2020)
87. J. Chang, J. W. N. Los, J. O. Tenorio-Pearl, N. Noordzij, R. Gourgues, A. Guardiani, J. R. Zichi, S. F. Pereira, H. P. Urbach, V. Zwiller, S. N. Dorenbos, and I. Esmaeil Zadeh, Detecting telecom single photons with $99.5_{-2.07}{}^{+0.5}$% system detection efficiency and high time resolution, *APL Photonics* 6(3), 036114 (2021)
88. B. Korzh, Q. Y. Zhao, S. Frasca, D. Zhu, E. Ramirez, E. Bersin, M. Colangelo, A. E. Dane, A. D. Beyer, J. Allmaras, E. E. Wollman, K. K. Berggren, and M. D. Shaw, in: 2018 Conference on Lasers and Electro-Optics (CLEO), pp 1–3
89. E. Taralli, M. de Wit, L. Gottardi, K. Nagayoshi, S. Visser, M. L. Ridder, H. Akamatsu, D. Vaccaro, M. P. Bruijn, J. R. Gao, and J. W. den Herder, Small size transition-edge sensors for future X-ray applications, *J. Low Temp. Phys.* 209(3–4), 256 (2022)
90. X. Xu, M. Rajteri, J. Li, S. Zhang, C. Pepe, J. Chen, H. Gao, Q. Li, W. Li, X. Li, M. Zhang, Y. Ouyang, and X. Wang, Investigation of Ti/Au transition-edge sensors for single-photon detection, *J. Low Temp. Phys.* 209(3–4), 372 (2022)
91. M. Guerra, M. Manso, S. Longelin, S. Pessanha, and M. L. Carvalho, Performance of three different Si X-ray detectors for portable XRF spectrometers in cultural heritage applications, *J. Instrum.* 7(10), C10004 (2012)
92. L. Brombal, S. Donato, F. Brun, P. Delogu, V. Fanti, P. Oliva, L. Rigon, V. Di Trapani, R. Longo, and B. Golosio, Large-area single-photon-counting CdTe detector for synchrotron radiation computed tomography: A dedicated pre-processing procedure, *J. Synchrotron Radiat.* 25(4), 1068 (2018)
93. Y. M. Ivanov, V. M. Kanevsky, V. F. Dvoryankin, V. V. Artemov, A. N. Polyakov, A. A. Kudryashov, E. M. Pashaev, and Z. J. Horvath, The possibilities of using semi-insulating CdTe crystals as detecting material for X-ray imaging radiography, *physica status solidi (c)* 0(3), 840 (2003)
94. C. Szeles, CdZnTe and CdTe materials for X-ray and gamma ray radiation detector applications, *physica status solidi (b)* 241(3), 783 (2004)
95. H. Wu, Y. Ge, G. Niu, and J. Tang, Metal halide perovskites for X-ray detection and imaging, *Matter* 4(1), 144 (2021)
96. Y. Zhou, J. Chen, O. M. Bakr, and O. F. Mohammed, Metal halide perovskites for X-ray imaging scintillators and detectors, *ACS Energy Lett.* 6(2), 739 (2021)
97. Y. Wu, J. Feng, Z. Yang, Y. Liu, and S. Liu, Halide perovskite: A promising candidate for next-generation X-ray detectors, *Adv. Sci. (Weinh.)* 10(1), 2205536 (2023)
98. K. Sakhatskyi, B. Turedi, G. J. Matt, E. Wu, A. Sakhatska, V. Bartosh, M. N. Lintangpradipto, R. Naphade, I. Shorubalko, O. F. Mohammed, S. Yakunin, O. M. Bakr, and M. V. Kovalenko, Stable perovskite single-crystal X-ray imaging detectors with single-photon sensitivity, *Nat. Photonics* 17(6), 510 (2023)
99. S. Shrestha, H. Tsai, and W. Nie, A perspective on the device physics of lead halide perovskite semiconducting detector for gamma and X-ray sensing, *Appl. Phys. Lett.* 122(8), 080501 (2023)
100. F. Zhang, C. Herman, Z. He, G. De Geronimo, E. Vernon, and J. Fried, Characterization of the $H_3D$ ASIC readout system and 6.0 $cm^3$ 3-D position sensitive CdZnTe detectors, *IEEE Trans. Nucl. Sci.* 59(1), 236 (2012)
101. F. Wang, T. Zhang, R. Xie, Z. Wang, and W. Hu, How to characterize figures of merit of two-dimensional photodetectors, *Nat. Commun.* 14(1), 2224 (2023)
102. M. A. Wolff, S. Vogel, L. Splitthoff, and C. Schuck, Superconducting nanowire single-photon detectors integrated with tantalum pentoxide waveguides, *Sci. Rep.* 10(1), 17170 (2020)
103. Z. Zhou, J. Lv, C. Tan, L. Yang, and Z. Wang, Emerging frontiers of 2D transition metal dichalcogenides in photovoltaics solar cell, *Adv. Funct. Mater.* 34, 2316175 (2024)
104. G. Z. Xu, W. J. Zhang, L. X. You, J. M. Xiong, X. Q. Sun, H. Huang, X. Ou, Y. M. Pan, C. L. Lv, H. Li, Z. Wang, and X. M. Xie, Superconducting microstrip single-photon detector with system detection efficiency over 90% at 1550 nm, *Photon. Res.* 9(6), 958 (2021)
105. H. Wang, P. Hu, Y. Xiao, X. Zhang, H. Zhou, W. Zhang, H. Li, L. You, and Z. Wang, Multispectral superconducting nanowire single-photon detector based on thickness-modulated optical film stack, *IEEE Photonics J.* 14(2), 6816304 (2022)
106. S. Das, D. Pandey, J. Thomas, and T. Roy, The role of graphene and other 2D materials in solar photovoltaics, *Adv. Mater.* 31(1), 1802722 (2019)

107. D. Salvoni, M. Ejrnaes, A. Gaggero, F. Mattioli, F. Martini, H. G. Ahmad, L. Di Palma, R. Satariano, X. Y. Yang, L. You, F. Tafuri, G. P. Pepe, D. Massarotti, D. Montemurro, and L. Parlato, *Phys. Rev. Applied* 18(1), 014006 (2022)
108. Y. Geng, W. Zhang, P. Z. Li, J. Q. Zhong, Z. Wang, W. Miao, Y. Ren, J. F. Wang, Q. J. Yao, and S. C. Shi, Improving energy detection efficiency of Ti-based superconducting transition-edge sensors with optical cavity, *J. Low Temp. Phys.* 199(1–2), 556 (2020)
109. X. Hu, D. Wu, H. Zhang, W. Li, D. Chen, L. Wang, X. Xiao, and S. Yu, High-speed and high-power germanium photodetector with a lateral silicon nitride waveguide, *Photon. Res.* 9(5), 749 (2021)
110. D. Thomson, A. Zilkie, J. E. Bowers, T. Komljenovic, G. T. Reed, L. Vivien, D. Marris-Morini, E. Cassan, L. Virot, J. M. Fédéli, J. M. Hartmann, J. H. Schmid, D. X. Xu, F. Boeuf, P. O'Brien, G. Z. Mashanovich, and M. Nedeljkovic, Roadmap on silicon photonics, *J. Opt.* 18(7), 073003 (2016)
111. M. R. Karim, N. Al Kayed, N. Jahan, M. S. Alam, and B. M. A. Rahman, Study of highly coherent mid-infrared supercontinuum generation in CMOS compatible Si-rich SiN tapered waveguide, *J. Lightwave Technol.* 40(13), 4300 (2022)
112. W. C. Hsu, N. Nujhat, B. Kupp, J. F. Jr Conley, and A. X. Wang, On-chip wavelength division multiplexing filters using extremely efficient gate-driven silicon microring resonator array, *Sci. Rep.* 13(1), 5269 (2023)
113. S. Schuler, J. E. Muench, A. Ruocco, O. Balci, D. Thourhout, V. Sorianello, M. Romagnoli, K. Watanabe, T. Taniguchi, I. Goykhman, A. C. Ferrari, and T. Mueller, High-responsivity graphene photodetectors integrated on silicon microring resonators, *Nat. Commun.* 12(1), 3733 (2021)
114. J. Mu, M. Dijkstra, J. Korterik, H. Offerhaus, and S. M. García-Blanco, High-gain waveguide amplifiers in $Si_3N_4$ technology via double-layer monolithic integration, *Photon. Res.* 8(10), 1634 (2020)
115. D. J. Blumenthal, R. Heideman, D. Geuzebroek, A. Leinse, and C. Roeloffzen, Silicon nitride in silicon photonics, *Proc. IEEE* 106(12), 2209 (2018)
116. J. Rönn, W. Zhang, A. Autere, X. Leroux, L. Pakarinen, C. Alonso-Ramos, A. Säynätjoki, H. Lipsanen, L. Vivien, E. Cassan, and Z. Sun, Ultra-high on-chip optical gain in erbium-based hybrid slot waveguides, *Nat. Commun.* 10(1), 432 (2019)
117. L. Feng, M. Zhang, J. Wang, X. Zhou, X. Qiang, G. Guo, and X. Ren, Silicon photonic devices for scalable quantum information applications, *Photon. Res.* 10(10), A135 (2022)
118. J. T. Kim and C. G. Choi, Graphene-based polymer waveguide polarizer, *Opt. Express* 20(4), 3556 (2012)
119. M. Kleinert, F. Herziger, P. Reinke, C. Zawadzki, D. de Felipe, W. Brinker, H. G. Bach, N. Keil, J. Maultzsch, and M. Schell, Graphene-based electroabsorption modulator integrated in a passive polymer waveguide platform, *Opt. Mater. Express* 6(6), 1800 (2016)
120. R. Hatai, F. Nakazaki, T. Nakayama, and T. Ishigure, Fabrication of Y-branched GI core polymer waveguide and its application to CWDM MUX device for multimode fiber, *J. Lightwave Technol.* 40(9), 2915 (2022)
121. Z. Ding, H. Wang, T. Li, X. Ouyang, Y. Shi, and A. P. Zhang, Fabrication of polymer optical waveguides by digital ultraviolet lithography, *J. Lightwave Technol.* 40(1), 163 (2022)
122. D. Sahin, A. Gaggero, Z. Zhou, S. Jahanmirinejad, F. Mattioli, R. Leoni, J. Beetz, M. Lermer, M. Kamp, S. Höfling, and A. Fiore, Waveguide photon-number-resolving detectors for quantum photonic integrated circuits, *Appl. Phys. Lett.* 103(11), 111116 (2013)
123. T. Gerrits, N. Thomas-Peter, J. C. Gates, A. E. Lita, B. J. Metcalf, B. Calkins, N. A. Tomlin, A. E. Fox, A. L. Linares, J. B. Spring, N. K. Langford, R. P. Mirin, P. G. R. Smith, I. A. Walmsley, and S. W. Nam, On-chip, photon-number-resolving, telecommunication-band detectors for scalable photonic information processing, *Phys. Rev. A* 84(6), 060301 (2011)
124. H. Wang, Y. Shi, Y. Zuo, Y. Yu, L. Lei, X. Zhang, and Z. Qian, High-performance waveguide coupled Germanium-on-silicon single-photon avalanche diode with independently controllable absorption and multiplication, *Nanophotonics* 12(4), 705 (2023)
125. J. Wu, H. Ma, C. Zhong, M. Wei, C. Sun, Y. Ye, Y. Xu, B. Tang, Y. Luo, B. Sun, J. Jian, H. Dai, H. Lin, and L. Li, Waveguide-integrated $PdSe_2$ photodetector over a broad infrared wavelength range, *Nano Lett.* 22(16), 6816 (2022)
126. N. Youngblood, C. Chen, S. J. Koester, and M. Li, Waveguide-integrated black phosphorus photodetector with high responsivity and low dark current, *Nat. Photonics* 9(4), 247 (2015)
127. Y. Yin, R. Cao, J. Guo, C. Liu, J. Li, X. Feng, H. Wang, W. Du, A. Qadir, H. Zhang, Y. Ma, S. Gao, Y. Xu, Y. Shi, L. Tong, and D. Dai, High-speed and high-responsivity hybrid silicon/black-phosphorus waveguide photodetectors at 2 μm, *Laser Photonics Rev.* 13(6), 1900032 (2019)
128. N. Flöry, P. Ma, Y. Salamin, A. Emboras, T. Taniguchi, K. Watanabe, J. Leuthold, and L. Novotny, Waveguide-integrated van der Waals heterostructure photodetector at telecom wavelengths with high speed and high responsivity, *Nat. Nanotechnol.* 15(2), 118 (2020)
129. P. L. Chen, Y. Chen, T. Y. Chang, W. Q. Li, J. X. Li, S. Lee, Z. Fang, M. Li, A. Majumdar, and C. H. Liu, Waveguide-integrated van der Waals heterostructure mid-infrared photodetector with high performance, *ACS Appl. Mater. Interfaces* 14(21), 24856 (2022)
130. J. Wu, M. Wei, J. Mu, H. Ma, C. Zhong, Y. Ye, C. Sun, B. Tang, L. Wang, J. Li, X. Xu, B. Liu, L. Li, and H. Lin, High-performance waveguide-integrated $Bi_2O_2Se$ photodetector for Si photonic integrated circuits, *ACS Nano* 15(10), 15982 (2021)
131. L. H. Zeng, D. Wu, S. H. Lin, C. Xie, H. Y. Yuan, W. Lu, S. P. Lau, Y. Chai, L. B. Luo, Z. J. Li, and Y. H. Tsang, Controlled synthesis of 2D palladium diselenide for sensitive photodetector applications, *Adv. Funct. Mater.* 29(1), 1806878 (2019)
132. S. Deng, A. V. Sumant, and V. Berry, Strain engineering in two-dimensional nanomaterials beyond graphene,

*Nano Today* 22, 14 (2018)

133. R. Frisenda, M. Drüppel, R. Schmidt, S. Michaelis de Vasconcellos, D. Perez de Lara, R. Bratschitsch, M. Rohlfing, and A. Castellanos-Gomez, Biaxial strain tuning of the optical properties of single-layer transition metal dichalcogenides, *npj 2D Mater. Appl.* 1, 10 (2017)
134. N. Tang, C. Du, Q. Wang, and H. Xu, Strain engineering in bilayer $WSe_2$ over a large strain range, *Microelectron. Eng.* 223, 111202 (2020)
135. W. Xu, J. D. Zheng, W. Y. Tong, J. L. Wang, Y. P. Shao, Y. K. Zhang, Y. F. Tan, and C. G. Duan, Strain-induced ferroelectric phase transition in group-V monolayer black phosphorus, *Adv. Quantum Technol.* 6(4), 2200169 (2023)
136. L. L. Li, R. Gillen, M. Palummo, M. V. Milošević, and F. M. Peeters, Strain tunable interlayer and intralayer excitons in vertically stacked $MoSe_2/WSe_2$ heterobilayers, *Appl. Phys. Lett.* 123(3), 033102 (2023)
137. D. Nayak and R. Thangavel, Tailoring the electronic and photocatalytic properties of $Mo_{1-x}W_xS_2$ monolayers via biaxial strain, *J. Mater. Sci.* 57(6), 4283 (2022)
138. S. Tareq, A. O. M. Almayyali, and H. R. Jappor, Prediction of two-dimensional AlBrSe monolayer as a highly efficient photocatalytic for water splitting, *Surf. Interfaces* 31, 102020 (2022)
139. R. Roldán, A. Castellanos-Gomez, E. Cappelluti, and F. Guinea, Strain engineering in semiconducting two-dimensional crystals, *J. Phys.: Condens. Matter* 27(31), 313201 (2015)
140. J. O. Island, A. Kuc, E. H. Diependaal, R. Bratschitsch, H. S. J. van der Zant, T. Heine, and A. Castellanos-Gomez, Precise and reversible band gap tuning in single-layer $MoSe_2$ by uniaxial strain, *Nanoscale* 8(5), 2589 (2016)
141. M. Hayashi, H. Yoshioka, H. Tomori, and A. Kanda, Theory of the strain engineering of graphene nanoconstrictions, *J. Phys. Soc. Jpn.* 90(2), 023701 (2021)
142. M. Chen, J. Xia, J. Zhou, Q. Zeng, K. Li, K. Fujisawa, W. Fu, T. Zhang, J. Zhang, Z. Wang, Z. Wang, X. Jia, M. Terrones, Z. X. Shen, Z. Liu, and L. Wei, Ordered and atomically perfect fragmentation of layered transition metal dichalcogenides via mechanical instabilities, *ACS Nano* 11(9), 9191 (2017)
143. C. Cho, J. Wong, A. Taqieddin, S. Biswas, N. R. Aluru, S. Nam, and H. A. Atwater, Highly strain-tunable interlayer excitons in $MoS_2/WSe_2$ heterobilayers, *Nano Lett.* 21(9), 3956 (2021)
144. Y. K. Ryu, F. Carrascoso, R. López-Nebreda, N. Agraït, R. Frisenda, and A. Castellanos-Gomez, Microheater actuators as a versatile platform for strain engineering in 2D materials, *Nano Lett.* 20(7), 5339 (2020)
145. Z. Chen, W. Luo, L. Liang, X. Ling, and A. K. Swan, Charge separation in monolayer $WSe_2$ by strain engineering: implications for strain-induced diode action, *ACS Appl. Nano Mater.* 5(10), 15095 (2022)
146. S. Manzeli, A. Allain, A. Ghadimi, and A. Kis, Piezoresistivity and strain-induced band gap tuning in atomically thin $MoS_2$, *Nano Lett.* 15(8), 5330 (2015)
147. J. Y. Juo, B. G. Shin, W. Stiepany, M. Memmler, K. Kern, and S. J. Jung, *In-situ* atomic level observation of the strain response of graphene lattice, *Sci. Rep.* 13(1), 2451 (2023)
148. P. Nemes-Incze, G. Kukucska, J. Koltai, J. Kürti, C. Hwang, L. Tapasztó, and L. P. Biró, Preparing local strain patterns in graphene by atomic force microscope based indentation, *Sci. Rep.* 7(1), 3035 (2017)
149. K. Wang, A. A. Puretzky, Z. Hu, B. R. Srijanto, X. Li, N. Gupta, H. Yu, M. Tian, M. Mahjouri-Samani, X. Gao, A. Oyedele, C. M. Rouleau, G. Eres, B. I. Yakobson, M. Yoon, K. Xiao, and D. B. Geohegan, Strain tolerance of two-dimensional crystal growth on curved surfaces, *Sci. Adv.* 5(5), eaav4028 (2019)
150. J. W. Christopher, M. Vutukuru, D. Lloyd, J. S. Bunch, B. B. Goldberg, D. J. Bishop, and A. K. Swan, Monolayer $MoS_2$ strained to 1.3% with a microelectromechanical system, *J. Microelectromech. Syst.* 28(2), 254 (2019)
151. Y. Y. Hui, X. Liu, W. Jie, N. Y. Chan, J. Hao, Y. T. Hsu, L. J. Li, W. Guo, and S. P. Lau, Exceptional tunability of band energy in a compressively strained trilayer $MoS_2$ sheet, *ACS Nano* 7(8), 7126 (2013)
152. R. Maiti, C. Patil, M. A. S. R. Saadi, T. Xie, J. G. Azadani, B. Uluutku, R. Amin, A. F. Briggs, M. Miscuglio, D. Van Thourhout, S. D. Solares, T. Low, R. Agarwal, S. R. Bank, and V. J. Sorger, Strain-engineered high-responsivity $MoTe_2$ photodetector for silicon photonic integrated circuits, *Nat. Photonics* 14(9), 578 (2020)
153. H. He, P. F. Yang, P. F. Zhang, G. Li, and T. C. Zhang, Single-photon source with sub-MHz linewidth for cesium-based quantum information processing, *Front. Phys.* 18(6), 61303 (2023)
154. A. Maccarone, K. Drummond, A. McCarthy, U. K. Steinlehner, J. Tachella, D. A. Garcia, A. Pawlikowska, R. A. Lamb, R. K. Henderson, S. McLaughlin, Y. Altmann, and G. S. Buller, Submerged single-photon LiDAR imaging sensor used for real-time 3D scene reconstruction in scattering underwater environments, *Opt. Express* 31(10), 16690 (2023)
155. X. Liu, J. Wang, L. Xiao, Z. Shi, X. Fu, and L. Qiu, Non-line-of-sight imaging with arbitrary illumination and detection pattern, *Nat. Commun.* 14(1), 3230 (2023)
156. R. Moya, A. C. Norris, T. Kondo, and G. S. Schlau-Cohen, Observation of robust energy transfer in the photosynthetic protein allophycocyanin using single-molecule pump–probe spectroscopy, *Nat. Chem.* 14(2), 153 (2022)
157. Q. Li, K. Orcutt, R. L. Cook, J. Sabines-Chesterking, A. L. Tong, G. S. Schlau-Cohen, X. Zhang, G. R. Fleming, and K. B. Whaley, Single-photon absorption and emission from a natural photosynthetic complex, *Nature* 619(7969), 300 (2023)
158. Z. Du, Y. Hu, N. Ali Buttar, and A. Mahmood, X-ray computed tomography for quality inspection of agricultural products: A review, *Food Sci. Nutr.* 7(10), 3146 (2019)
159. J. Jiang, M. Xiong, K. Fan, C. Bao, D. Xin, Z. Pan, L. Fei, H. Huang, L. Zhou, K. Yao, X. Zheng, L. Shen, and F. Gao, Synergistic strain engineering of perovskite single crystals for highly stable and sensitive

X-ray detectors with low-bias imaging and monitoring, *Nat. Photonics* 16(8), 575 (2022)

160. G. H. Zuo, Y. C. Zhang, G. Li, P. F. Zhang, P. F. Yang, Y. Q. Guo, S. Y. Zhu, and T. C. Zhang, 10-Hertz squeezed light source generation on the cesium $D_2$ line using single photon modulation, *Front. Phys.* 18(3), 32301 (2023)
161. Z. P. Li, X. Huang, Y. Cao, B. Wang, Y. H. Li, W. Jin, C. Yu, J. Zhang, Q. Zhang, C. Z. Peng, F. Xu, and J. W. Pan, Single-photon computational 3D imaging at 45 km, *Photon. Res.* 8(9), 1532 (2020)
162. X. T. Fang, P. Zeng, H. Liu, M. Zou, W. Wu, Y. L. Tang, Y. J. Sheng, Y. Xiang, W. Zhang, H. Li, Z. Wang, L. You, M. J. Li, H. Chen, Y. A. Chen, Q. Zhang, C. Z. Peng, X. Ma, T. Y. Chen, and J. W. Pan, Implementation of quantum key distribution surpassing the linear rate-transmittance bound, *Nat. Photonics* 14(7), 422 (2020)
163. J. P. Chen, C. Zhang, Y. Liu, C. Jiang, W. Zhang, X. L. Hu, J. Y. Guan, Z. W. Yu, H. Xu, J. Lin, M. J. Li, H. Chen, H. Li, L. You, Z. Wang, X. B. Wang, Q. Zhang, and J. W. Pan, Sending-or-not-sending with independent lasers: Secure twin-field quantum key distribution over 509 km, *Phys. Rev. Lett.* 124(7), 070501 (2020)
164. S. Wang, Z. Q. Yin, D. Y. He, W. Chen, R. Q. Wang, P. Ye, Y. Zhou, G. J. Fan-Yuan, F. X. Wang, W. Chen, Y. G. Zhu, P. V. Morozov, A. V. Divochiy, Z. Zhou, G. C. Guo, and Z. F. Han, Twin-field quantum key distribution over 830-km fibre, *Nat. Photonics* 16(2), 154 (2022)